



Defence Research and
Development Canada

Recherche et développement
pour la défense Canada

Copy No:



Lidar Signal Depolarization by Solid Targets and its application to Terrain Mapping and 3D Imagery

Xiaoying Cao and Robert Bernier

Prepared by:

Les instruments optiques du Saint-Laurent inc.
17500 Montée Gascon
Mirabel, (Québec)
J7J 2C5

Project Manager: Robert Bernier, 514-944-2526
Contract Number: W7701-071506
Contract Scientific Authority: Gilles Roy, 418-844-4000 (4335)

The scientific or technical validity of this Contract Report is entirely the responsibility of the Contractor and the contents do not necessarily have the approval or endorsement of Defence R&D Canada.

Defence R&D Canada – Valcartier

Contract Report
DRDC Valcartier CR 2011-236
March 2011

Canada 

Lidar Signal Depolarization by Solid Targets and its application to Terrain Mapping and 3D Imagery

Xiaoying Cao and Robert Bernier

Prepared by:

Les instruments optiques du Saint-Laurent inc.
17500 Montée Gascon
Mirabel, (Québec)
J7J 2C5

Project Manager: Robert Bernier 514-944-2526

Contract Number: W7701-071506

Contract Scientific Authority: Gilles Roy, 418-844-4000 (4335)

The scientific or technical validity of this Contract Report is entirely the responsibility of the Contractor and the contents do not necessarily have the approval or endorsement of Defence R&D Canada

Defence R&D Canada – Valcartier

Contract Report

DRDC Valcartier CR 2011-236

March 2011

Principal Author

Xiaoying Cao

Approved by

Original signed by Xiaoying Cao

Xiaoying Cao

Approved for release by

Original signed by Gilles Roy

Gilles Roy

Defence Scientist

Work performed under: ARP 13MG05: Active Imaging in the SWIR Band for Northern Surveillance and Reconnaissance – Atmospheric effects

© Her Majesty the Queen in Right of Canada, as represented by the Minister of National Defence, 2011

© Sa Majesté la Reine (en droit du Canada), telle que représentée par le ministre de la Défense nationale, 2011

Abstract

Solid targets are used for calibration of lidars for atmospheric studies. Solid targets make up the surface of the Earth and thus they reflect light back to lidars being used for Terrain Mapping. Experience and theory show that if polarization effects are not accounted for in the lidar calibration process, important systematic errors will result. In this report, the experimental study of various solid targets used in lidar calibration shows that none of these truly meets the expectation of being a true lambertian reflector, that is a perfectly isotropically reflector and a totally depolarizing one as well. On another hand, Terrain Mapping, an important lidar application, is still under development. Lidars used in Terrain Mapping yield massive volumes of data. The automatic processing of these data still is an issue and experience shows that adding more features to the lidar signal, over and above the range information, would be a most valuable contribution to automated processing. The work reported in this report is about the use of the polarization signature of solid targets in Terrain Mapping. First, experimental results are compared to the theoretical predictions of the pBRDF theory. The analysis of the results shows that the polarization signature from solid targets may be expected to be a reliable and repeatable feature to add to the data processing. Then, it is shown that discrimination between targets may be obtained by use of their polarization signature. This opens up the way for an improved automation of data processing.

Résumé

Des cibles solides sont utilisées pour la calibration de lidars dédiés aux études atmosphériques. Des cibles solides sont aussi ce qui forme la surface de la Terre, donc ce qui reflète l'énergie vers les lidars utilisés en Cartographie de la Terre. L'expérience et la théorie montrent que d'importantes erreurs systématiques résulteront si les effets de la polarisation ne sont pas pris en compte lors de la calibration des lidars. Dans ce rapport, l'analyse des mesures expérimentales acquises sur des cibles solides couramment utilisées en calibration de lidars montre qu'aucune d'entre elles ne peut être vue comme un réflecteur lambertien, c'est-à-dire un réflecteur isotrope et complètement dépolarisant. Sur un autre plan, la cartographie de terrain est une application lidar en plein développement. Les lidars utilisés à cet escient produisent un énorme volume de données. L'automatisation du traitement de ces données est encore problématique et l'expérience montre que l'ajout d'autres informations dans le signal lidar, à part la distance, serait d'une grande aide. Ce rapport porte sur l'application des mesures en polarisation à la cartographie de terrain. Premièrement, les résultats expérimentaux sont comparés aux prédictions faites par la théorie pBRDF. L'analyse des résultats montre que la signature en polarisation de cibles solides peut être une caractéristique fiable et répétable à ajouter au signal lidar. Ensuite, il est montré qu'il est possible de discriminer entre des cibles solides au moyen de leur signature en polarisation. Ceci ouvre la voie vers une amélioration sensible du traitement automatique des données.

This page intentionally left blank.

Executive summary

Lidar Signal Depolarization by Solid Targets and its application to Terrain Mapping and 3D Imagery

Cao, X.; Bernier, R.; DRDC Valcartier CR 2011-236; Defence R&D Canada – Valcartier; March 2011.

Introduction or background: This report bears on the application of the polarization signature of solid targets to two different fields of activity of the lidar technology: the calibration of lidars for atmospheric studies and the automated processing of data for lidars used in Terrain Mapping.

In order to allow the comparison of data acquired from different ground, air or space based lidars, their output needs to be precisely calibrated. For this, some specific solid targets are used. The assumption most of the time done about those targets is that they are true lambertian reflectors. This report is about measurements which have been made to verify the lambertian character of various solid targets used in lidar calibration.

Lidars are more and more used in Terrain Mapping because they directly yield the information of height above ground and, also, because they can, to a certain level, pass across the forest canopy. Lidars used in Terrain Mapping yield large volumes of data. The automation of the data processing would be made much more efficient if more information than just range could be made available from the lidar signal. The works reported in this report were done to verify whether the polarization effect of solid targets could be such a valuable feature to add to the Terrain Mapping lidar signal.

Results: For lidar calibration, the results reported here show that no solid target currently recommended for lidar calibration is a true lambertian reflector.

For Terrain Mapping and 3D Imagery, the results reported here show that all of the more than 60 different materials studied here behave in a way that validates four predictions that can be made out of the pBRDF theory. Hence, their polarization signature is shown to be a reliable feature. Moreover, the results show that it is possible to discriminate between different types of materials by using their polarization signature.

Significance: If the measure of polarization is added in Terrain Mapping and 3D imagery, it is thought that an important gain will be made in automatic processing of the data, which is the place where a breakthrough needs to be achieved.

Future plans: More precise and thorough pBRDF measurements should be done on a larger bank of different types of materials.

Sommaire

Lidar Signal Depolarization by Solid Targets and its application to Terrain Mapping and 3D Imagery

Cao, X.; Bernier, R.; DRDC Valcartier CR 2011-236; R & D pour la défense Canada – Valcartier; Mars 2011.

Introduction ou contexte: Ce rapport porte sur l'application de la polarisation de cibles solides à deux champs d'étude de la technologie lidar : la calibration des lidars utilisés en études atmosphériques et l'automatisation du traitement des données recueillies par des lidars en cartographie de la Terre.

Si l'on veut pouvoir comparer les données de lidars basés au sol ou aéroportés, il faut avoir calibré précisément leur signal. Des cibles solides spécifiques sont utilisées à cette fin. On fait en général l'hypothèse que ces cibles agissent comme de parfaits réflecteurs lambertiens. Ce rapport porte sur des mesures qui ont été faites dans le but de valider cette hypothèse eu égard à différentes cibles solides couramment recommandées pour la calibration des lidars.

Des lidars sont de plus en plus souvent utilisés en cartographie de la Terre parce qu'ils donnent directement l'information de hauteur en plus de traverser le couvert forestier. Ces lidars génèrent de larges volumes de données. L'automatisation du traitement de ces données serait plus efficace si de l'information autre que la seule distance pouvait être recueillie dans le signal lidar. Ce rapport porte sur des travaux menés pour vérifier si la signature en polarisation des cibles solides au sol pouvait être une information supplémentaire utile et fiable.

Résultats: Les résultats rapportés ici sont à l'effet qu'aucune des cibles solides recommandées pour la calibration des lidars n'est un parfait réflecteur lambertien.

Pour la cartographie et l'imagerie 3D, l'étude de plus de 60 matériaux différents montrent que leur signature en polarisation est prédictible dans le cadre de la théorie pBRDF et peut donc être considérée comme une information fiable. De plus, il est montré que les résultats permettent de discriminer entre les différents types de matériaux.

Importance: Si la mesure en polarisation est ajoutée aux données lidars pour la cartographie et l'imagerie 3D, un gain appréciable pourrait être réalisé dans le domaine du traitement des données, là où une avancée est justement requise de façon importante.

Perspectives: Des données plus précises rapportées à la théorie pBRDF devraient être recueillies sur une banque encore plus large de matériaux divers.

Table of contents

Abstract	i
Résumé	i
Executive summary	iii
Sommaire	iv
Table of contents	v
List of figures	vi
List of tables	viii
Acknowledgements	ix
1 INTRODUCTION	1
2 REVIEW OF THE pBRDF THEORY	3
3 EXPERIMENTAL SETUP.....	8
4 SOLID TARGETS FOR LIDAR CALIBRATION.....	14
4.1 Background	14
4.2 RESULTS FOR LIDAR CALIBRATION SOLID TARGETS	15
4.2.1 Spectralon targets	16
4.2.2 Sandpaper Targets.....	19
4.3 CONCLUSIONS ON HARD TARGETS FOR LIDAR CALIBRATION	23
5 SOLID TARGETS FOR LIDAR TERRAIN MAPPING AND 3D IMAGERY	25
5.1 BACKGROUND	25
5.2 RESULTS ON THE pBRDF OF SOME SOLID TARGETS	26
5.2.1 Methodology	26
5.2.2 Results for the dependence of depolarization on reflectivity	28
5.2.3 Results for the dependence of depolarization on incidence angle.....	35
5.2.4 Results for the dependence of depolarization on wavelength	42
5.2.5 Conclusions about the validity of the microfacet pBRDF theory	46
5.3 DISCRIMINATION OF SOLID TARGETS BY POLARIZATION	46
5.3.1 The Mahalanobis distance.....	47
5.3.2 Results for the discrimination between solid targets.....	49
6 GENERAL CONCLUSIONS.....	55
7 References	56

List of figures

Figure 1 : Schematics of the optical layout of the MFOV Dual-Polarization Imaging Lidar setup..	8
Figure 2 : Schematics of the optical layout of the Dual-Polarization Non-Imaging Lidar setup	9
Figure 3 : Effect of the scanner mirrors on the polarization state of the light at emission	10
Figure 4-a : Image of the calibration target reflectivity before laser beam uniformity calibration	12
Figure 4-b : Image of the calibration target reflectivity after laser beam uniformity calibration..	12
Figure 5 : Wavelength dependence of the linear depolarization ratio of various samples of Spectralon materials.....	16
Figure 6-a : Incidence angle dependence of the linear depolarization ratio of various samples of Spectralon materials at wavelength 355 nm	17
Figure 6-b : Incidence angle dependence of the linear depolarization ratio of various samples of Spectralon materials at wavelength 532 n.	18
Figure 6-c : Incidence angle dependence of the linear depolarization ratio of various samples of Spectralon materials at wavelength 1064 nm	18
Figure 6-d : Incidence angle dependence of the linear depolarization ratio of various samples of Spectralon materials at wavelength 1570 nm	19
Figure 7 : Wavelength dependence of the linear depolarization ratio of various samples of sandpapers.....	20
Figure 8-a : Incidence angle dependence of the linear depolarization ratio of various samples of sandpapers at wavelength 355 nm.	21
Figure 8-b : Incidence angle dependence of the linear depolarization ratio of various samples of sandpapers at wavelength 532 nm.	21
Figure 8-c : Incidence angle dependence of the linear depolarization ratio of various samples of sandpapers at wavelength 1064 nm.	22
Figure 8-d : Incidence angle dependence of the linear depolarization ratio of various samples of sandpapers at wavelength 1570 nm.	22
Figure 9 : Relationship between depolarization ratio and reflectivity for sandpapers and some other specimen at 532 nm. The figure also shows that the depolarization ratio increases with incidence angle.	23
Figure 10 : Wooden black panel with diverse specimen of insulation materials.	27
Figure 11 : Dependence of the depolarization on the reflectivity of insulation materials at 532 nm.	30
Figure 12 : Dependence of the depolarization on the reflectivity of woods at 532 nm.....	31
Figure 13 : Dependence of the depolarization on the reflectivity of metals at 532 nm.....	31
Figure 14-a : Dependence of the depolarization on the reflectivity of environmental materials at 532 nm (all specimen shown).	32

Figure 14-b : Dependence of the depolarization on the reflectivity of environmental materials at 532 nm (smooth metallic soda can, sample 5, removed).	32
Figure 15 : Dependence of the depolarization on the reflectivity of sandpapers, paper and cardboard materials at 532 nm.	33
Figure 16-a : Dependence of the depolarization on the reflectivity of composites materials at 532 nm (all specimen shown).	34
Figure 16-b : Dependence of the depolarization on the reflectivity of composites materials at 532 nm (specimen 8 and 9 removed).	34
Figure 17 : Dependence of the depolarization on the reflectivity of sands and grass at 532 nm. .	35
Figure 18 : Insulation targets linear depolarization ratio variation with incident angle at each wavelength. (a) 355 nm, (b) 532 nm, (c) 1064 nm and (d) 1570 nm.	37
Figure 19 : Sandpapers linear depolarization ratio variation with incident angle at each wavelength. (a) 355 nm, (b) 532 nm, (c) 1064 nm and (d) 1570 nm.	38
Figure 20 : Sands and concrete linear depolarization ratio variation with incident angle at each wavelength. (a) 355 nm, (b) 532 nm, (c) 1064 nm and (d) 1570 nm.	39
Figure 21 : Woods linear depolarization ratio variation with incident angle at each wavelength. (a) 355 nm, (b) 532 nm, (c) 1064 nm and (d) 1570 nm.	40
Figure 22 : Metals linear depolarization ratio variation with incident angle at each wavelength. (a) 355 nm, (b) 532 nm, (c) 1064 nm and (d) 1570 nm.	41
Figure 23 : Composites linear depolarization ratio variation with incident angle at each wavelength. (a) 355 nm, (b) 532 nm, (c) 1064 nm and (d) 1570 nm.	42
Figure 24 : Wood targets linear depolarization ratio variation with wavelength at (a) 0° and (b) 30°	43
Figure 25 : Insulation targets linear depolarization ratio variation with wavelength at (a) 0° and (b) 30°	43
Figure 26 : Sandpapers targets linear depolarization ratio variation with wavelength at (a) 0° and (b) 30°	44
Figure 27 : Metallic targets linear depolarization ratio variation with wavelength at (a) 0° and (b) 30°	44
Figure 28 : Composite targets linear depolarization ratio variation with wavelength at (a) 0° and (b) 30°	45
Figure 29 : Sands and concrete targets linear depolarization ratio variation with wavelength at (a) 0° and (b) 35°	45
Figure 30 : Solid Targets discrimination with two wavelengths	52

List of tables

Table 1 : Lists of Targets for the study of depolarization vs reflectivity.....	28
Table 2 : Lists of Targets for the study of depolarization vs angle and wavelength	35
Table 3 : List of Targets for the study of the discrimination possibilities of a polarimetric lidar system50	
Table 4 : Results of calculations for the discrimination between targets using the Mahalanobis distance	51
Table 5 : Results of calculations for the discrimination between types of materials using the Mahalanobis distance.....	53

Acknowledgements

Special thanks go to Gregoire Tremblay of AEREX Avionics Inc., Simon Roy and Christian Laflamme both from RDDC-Valcartier.

This page intentionally left blank.

1 INTRODUCTION

Over the last two decades, the Lidar technology has been put to many uses. One branch of research to which lidar has been applied is atmospheric studies. Another one has more to do with geodetic and geophysical studies. A more recent application, which is fast developing, is 3D scene imagery for either military or civilian applications.

This report bears on the subject of effects of polarization of light that occur when light is reflected off the surface of solid targets. Such solid targets have been used for the calibration of lidars applied to atmospheric studies. Also, solid targets make up the surface of the earth from which lidar returns are analyzed in view of building Terrain Models or Terrain Mappings. For these reasons, the results of this research may have relevance for the two fields of application introduced earlier: atmospheric studies and geodetic studies.

Calibration of the sensitivity of a lidar must be performed in order to adequately analyze the lidar signal in terms of scattering off aerosols as must be done in atmospheric studies. When this calibration is obtained through the analysis of the signal recorded by a lidar aimed at a calibration solid target, the hypothesis most often done, based on the appropriate choice of target, is that the target was a true lambertian reflector.

The definition of a true lambertian reflector has two sides to it: first, that it reflects isotropically in all directions and, second, that it completely depolarizes the light that was incident at it.

This report will add more experimental confirmation to the important finding that could be summarized as saying that ‘no reflector is a true lambertian reflector’¹⁻². And this means that polarization effects must always be taken account of when calibrating a lidar and analyzing the signal of a lidar.

The application of the lidar technology to terrain mapping has seen an important increase of activity over the last decade. The reason behind this growing interest is that the lidar technology has the capability to give absolute values of difference of levels between adjacent parcels of terrain. On terrains where there is vegetation, the lidar signal will even allow some penetration of the canopy, hence yielding vegetation height above terrain as well as terrain surface model. Over urban areas, the lidar signal can be used to measure the distribution and height of buildings for urbanistic applications. In all cases, the analysis of the lidar data requires that the cloud of lidar points first be separated between ground and non ground points. Many algorithms have been applied for achieving this binary classification, and most of them rely on some models of physically possible terrain slopes. In all currently existing algorithms and software, identification of what are called break-lines in the terrain image is a difficulty and most often requires the interactive input from an expert at critical points of the image processing. Experience has shown that the addition of the intensity of the signal as another feature of the lidar signal, next to range, always adds significant information in view of this decision making. It brings the image processing algorithm a step closer to the ultimate aim of a fully automated treatment.

The application of lidar to 3D fine resolution imagery has also been emerging recently. In this case also, image segmentation and object recognition and classification are demanding tasks.

This report is on the polarization effects of solid targets as another and interesting feature that could be added to the lidar signal in view of getting even closer to full automation of lidar data analysis for terrain mapping. For instance, the fact that man-made objects tend not to exhibit circular polarization could be of interest for automated detection of breaklines [ref. 3, p. 100].

The report will proceed as follows. In section 2, a review of the theory of polarimetric Bi-directional Reflectance Distribution Functions (pBRDF) is given. Next, in section 3, presentation is made of the experimental setups that have been used for the works reported here. A brief discussion of the data processing is included in that section as well.

In Section 4, the topic of solid targets for lidar calibration is discussed. It starts by a review of the historical background. Then, the results of field measurements are presented and discussed. That part ends with some conclusions where the importance of reference targets fully calibrated with respect to polarization effects is enhanced.

In Section 5, the application of the polarization signature of solid targets to the field of Terrain Mapping is developed. If the polarimetric lidar is to gain acceptance in the field of Terrain Mapping, it needs to be shown that there is good ground for thinking that the polarization signature of typical materials will be repeatable. In this part of the report, much experimental data is first analyzed in order to show that solid targets reliably conform to what the dominant microfacet pBRDF theory predicts: hence, the information out of a lidar could safely be applied to objects classification. Second, the analysis of the polarization content of the experimental data is shown to allow the discrimination and classification of types of objects that can be found at the surface of the earth: hence, classification could be reliably achieved in view of an adequate and hopefully totally automated image processing.

Finally, in section 6, we present some general conclusions.

2 REVIEW OF THE pBRDF THEORY

The acronym BRDF refers to the Bi-directional Reflectance Distribution Function which, succinctly, gives the information about the probability of light incident at an object surface from some incident direction to be reflected in any other predetermined direction. The pBRDF is the polarimetric version of the BRDF and will further inform about the (de)polarizing effect of that object surface interacting with the incoming light. The theoretical background of the pBRDF has recently been reviewed by James R. Shell II and John R. Schott³.

The BRDF theory aims at explaining and predicting the diffuse vs specular reflection phenomenology whereas various types of reflection are seen: specular, nearly specular, nearly diffuse and totally diffuse.

The BRDF gives, for each possible direction, the ratio of the radiance L scattered off the object surface in the direction (θ_r, ϕ_r) to the irradiance E incident on that same surface from the direction (θ_i, ϕ_i) . A general form of the BRDF makes it a function of the four angles just introduced.

$$f(\theta_r, \phi_r, \theta_i, \phi_i) = \frac{L(\theta_r, \phi_r)}{E(\theta_i, \phi_i)} \quad (\text{eq. 1})$$

The exact definitions for L and E will be found in the Nonconventional Exploitation Factors (NEF) Modeling document listed in reference⁴. Basically, the irradiance E is the radiance L incident on the surface multiplied by the cosine of the incident angle in order to account for the projection at an angle of the incident beam onto the object surface. It must be noted that L and E are defined as the result of an integral over all the wavelengths comprising the illuminating beam. In all that follows here, monochromatism at the lidar wavelength will be assumed.

Using the equation 1, it will be seen that the power collected in the direction (θ_r, ϕ_r) over a solid angle dw_r given by the geometry of the receiver with respect to the source, can be written as

$$P(\theta_r, \phi_r, \theta_i, \phi_i) = \int f(\theta_r, \phi_r, \theta_i, \phi_i) \cdot L(\theta_i, \phi_i) \cdot \cos \theta_i \cdot dw_r \quad (\text{eq. 2})$$

The function $f(\theta_r, \phi_r, \theta_i, \phi_i)$ is the BRDF of the surface under consideration and it characterizes the effect (absorption and scattering) of that surface on an incident light beam.

Since Torrance and Sparrow (1967)⁵, a detailed model for the BRDF $f(\theta_r, \phi_r, \theta_i, \phi_i)$ of roughened surfaces has started to develop. These models all rely on a geometrical optics analysis and, as such, remain valid under the condition that the ratio σ / λ of the rms size σ of the facets to the incident light wavelength is larger than 1.

Their model describes a material surface as made of a collection of microfacets variously tilted with respect to the incident beam. The statistics of the angles and sizes of the facets is the most critical feature characterizing any material with regards to light reflection. Each single facet is modelled as obeying the Fresnel equation $F(\psi, \hat{n})$ for reflection where ψ is the angle between the facet normal and the incident beam and \hat{n} is the complex index of refraction which integrates both the effects of absorption and refraction of the facet at the prescribed wavelength.

Since one facet can either shine its reflected light towards another facet or, to the contrary, prevent incident light from reaching some other facet, it is custom practice since Torrance and Sparrow to introduce another function within the BRDF to account for these possible masking/shadowing effects arising from the geometrical details of the surface. The generic function for these effects is $G(\psi_p, \theta_p)$ where ψ_p is the angle that the individual facet makes with the mean surface normal and θ_p is the angle of incidence of the beam with respect to the mean surface normal.

Since these works by Torrance and Sparrow, the BRDF will thus be modelled as the result of a Fresnel equation and a geometrical attenuation (masking/shadowing) factor. The effect of each facet will be integrated to build the macroscopic BRDF by accounting for the exact probability of each facet.

$$f(\theta_r, \phi_r, \theta_i, \phi_i) = F(\psi, \hat{n}) \bullet G(\psi_p, \theta_p) \quad (\text{eq. 3})$$

Most of the works since Torrance and Sparrow has consisted in developing new versions of the function $G(\psi_p, \theta_p)$. A recent review of these models can be found in Yinlong Sun (2007)⁶.

According to ref [3], it was in a paper by Flynn and Alexander (1995)⁷ that a polarimetric version of the BRDF of equation 3 was first introduced. The polarimetric version of the BRDF will be referred to from now on as the pBRDF. Basically, that equation would obey the general form

$$\vec{L} = f\vec{E} \quad (\text{eq. 4})$$

where $\vec{L} = L\vec{S}_{out}$ and $\vec{E} = E\vec{S}_{in}$ in which \vec{S}_{out} and \vec{S}_{in} are normalized Stokes vectors describing the polarization states of the scattered and incident light respectively while the functions L and E carry the geometrical factors relative to observation and illumination respectively. Schott's presentation has been selected for its brevity and clarity. The Stokes vectors are quadrivectors. Therefore, the BRDF function f will be replaced by a 4 X 4 Mueller matrix in its polarimetric version pBRDF.

$$\vec{L} = L \begin{bmatrix} S_0 \\ S_1 \\ S_2 \\ S_3 \end{bmatrix}_{out} = \begin{bmatrix} f_{00} & f_{01} & f_{02} & f_{03} \\ f_{10} & f_{11} & f_{12} & f_{13} \\ f_{20} & f_{21} & f_{22} & f_{23} \\ f_{30} & f_{31} & f_{32} & f_{33} \end{bmatrix} E \begin{bmatrix} S_0 \\ S_1 \\ S_2 \\ S_3 \end{bmatrix}_{in} \quad (\text{eq. 5})$$

This polarimetric version of the multifacet scattering model is well developed in Priest and Germer (2000)⁸, Conant and Iannarilli (2002)⁹ and Priest and Meier (2002)¹⁰.

The polarimetric lidar version of all these models could be summarized as

$$\vec{E}_D = M_D f M_T \vec{E}_T \quad (\text{eq. 6})$$

where \vec{E}_T is the Stokes vector of the lidar laser source, M_T is the Mueller matrix of the lidar transmitting optics, f is the material scattering Mueller matrix, M_D is the Mueller matrix of the lidar detection optics and, finally, \vec{E}_D is the Stokes vector of the detected light.

In this equation, each one of the 16 Mueller matrix f elements will be a function of the Fresnel reflectance $F(\psi, \hat{n})$ and of the masking/shadowing geometrical factor $G(\psi_p, \theta_p)$, both depending on the four angles introduced above, plus material dependent polarization factors. In all models, the masking/shadowing geometrical attenuation factor $G(\psi_p, \theta_p)$ is dependent upon the ratio of the rms characteristic size of the microfacets to the illumination wavelength: σ/λ . On their side, the material dependent polarization factors are mostly described in terms of rotation matrices which, depending on the angle of the facet with respect to the incident polarization vector will have this vector to be rotated. Other dependences on the material are related to the complex refractive index \hat{n} of the material. For ease of representation of this somehow complex phenomenon, let us summarize all this below:

$$f_{ij} = F(\theta_r, \phi_r, \theta_i, \phi_i, \hat{n}) \bullet G(\theta_r, \phi_r, \theta_i, \phi_i, \sigma) \bullet R(\theta_r, \phi_r, \theta_i, \phi_i) \quad (\text{eq. 7})$$

For whatever roughened surface, there will be depolarization effects, would they be due solely to the polarization rotation matrix which is part of equation 7.

However, these will greatly depend on the ratio σ/λ of the rms size of the facets to the wavelength. For the same value of σ , the surface would appear smoother for larger values of λ and the diffusivity and depolarization effects of the surface should diminish. The experimental works reported in Stagg and Charalampopoulos (1991)¹¹ as well as in Oppenheim and Feiner (1995)¹² show that the more the ratio $\sigma/\lambda \gg 1$, the more the depolarization effects caused by rough surfaces will tend to conform to what is predicted by the Fresnel reflectance function only:

the surface tends to act as tilted plane mirrors when the facets are large with respect to the wavelength.

For a lidar in the backscatter configuration as will be assumed here for the two applications discussed in this paper (atmospheric studies and terrain mapping), the above prediction boils down to stating that, for larger values of λ , the depolarization effects should diminish (prediction P1). The reason is that, in the backscatter configuration, all the light returning to the lidar is at first sight deemed to be mostly due to facets tilted towards the lidar and thus presenting a 0 degree angle of incidence. Since, for larger values of λ , the depolarization effects would tend to be those predicted by the Fresnel reflectance, it ensures that, with a null incidence angle, those effects should tend to be weak or null.

In the backscatter configuration, any depolarization should thus come not from single scattering events at any 0 degree tilted facet but rather from multiple scattering events at the surface or even from within the surface. This effect would then appear as contradictory to the one just discussed above. Here, with smaller values of the ratio σ / λ because of smaller facets, a larger number of multiple scattering events is predicted and depolarization should increase (prediction P2).

A material with a large absorption coefficient should prevent multiple scattering events to occur. The returning light would thus come from first surface reflection events. As a consequence, rough surfaces of highly absorbing materials should be weak depolarizers. To the contrary, rough surfaces of weakly absorbing, that is highly reflecting, materials should be strong depolarizers. For rough surfaces, we should thus observe a proportionality relation between reflectivity and depolarization (prediction P3). This effect will be referred to from now on as the Umov effect, by the name of the Russian astronomer who stated in 1905 that the degree of polarization of the light scattered by astronomical objects like the moon tends to be inversely proportional to their albedo [in ref. 3, page 73].

A further prediction that we could extract from the last analysis is that the depolarization by a highly reflecting rough surface should increase with increasing incidence angle, at least slightly (prediction P4). The reason for this is that, the larger the incidence angles between the laser beam and the mean surface normal, the more likely it will be for many scattering events to have occurred for light to return in the backscatter direction, each of these scattering events introducing some more depolarization.

Let us summarize here below what generic predictions can be made about depolarization by rough surfaces for a lidar in the backscatter configuration:

P1) for a given surface roughness, the depolarization should diminish as the wavelength increases;

P2) for the same wavelength, the depolarization should however increase as the roughness rms size diminishes, since this will augment the probability for multiple scattering events;

P3) we expect the Umov effect whereby depolarization by rough surfaces increases with their reflectivity or albedo and

P4) for highly reflecting rough surfaces, the depolarization should increase with increasing incidence angles.

It will be the task of the experimental work reported here to investigate the validity of these generic predictions that we can be led to by the various pBRDF models.

3 EXPERIMENTAL SETUP

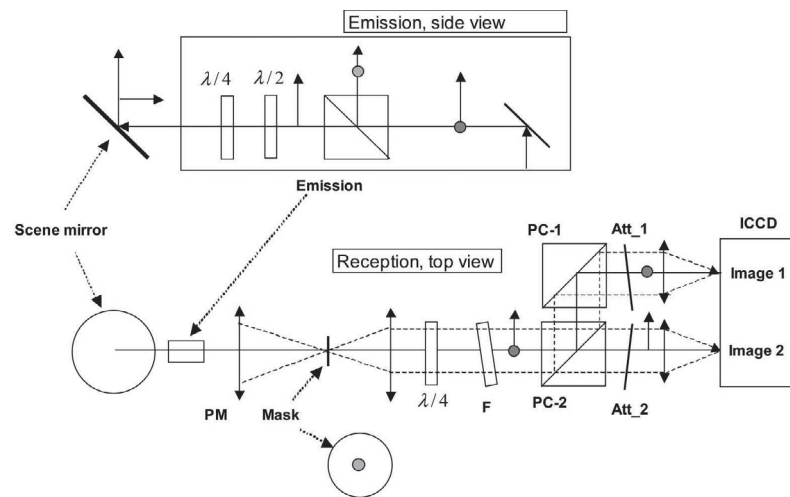
As stated in the introduction, this report will be separated in two parts. Part I will study the depolarization by some special solid targets from the point of view of their application to the calibration of lidars for atmospheric studies. Part II will study the depolarization by larger classes of solid targets from the point of view of the application of polarimetric lidars to Lidar Terrain Mapping.

In either case, the experimental setups that will be used are of two sorts which are very intimately related. Hence, their presentation here prior to entering the specifics of Part I and Part II topics.

The two different experimental setups will be referred to as the MFOV Dual-Polarization Imaging Lidar setup and the Dual-Polarization Non-Imaging Lidar setup.

The MFOV Dual-Polarization Imaging Lidar setup was equipped with an Intensified Charge Coupled Detector (ICCD) area camera. For retrieving the energy collected within a specific Field of View (FOV), integration of the energy over the many pixels comprising the FOV has to be performed.

Figure 1 is a schematic of the MFOV Dual-Polarization Imaging Lidar optical setup.



PM: 20 cm parabolic mirror; F: interference filter; PC_1 and PC_2: polarization cube beam splitter; Att_1 and Att_2: attenuators

Figure 1: Schematics of the optical layout of the MFOV Dual-Polarization Imaging Lidar setup

The status of polarized light transmitted by the lidar is controlled by adjusting the quarter and half-wave plates in the emission arm of the instrument. By rotating the half-wave plate by 45° in one or the other direction, the linear polarization of the laser light can be oriented either horizontally or vertically. By rotating the quarter-wave plate by $\pm 45^\circ$, this linear polarization state can be made into a left or right circular polarization state. The results reported in this paper will refer to linear polarization only.

In the reception arm of the instrument, the use of the quarter-wave plate is important. Circularly polarized incoming light will be reconverted to linearly polarized by the appropriate rotation by $\pm 45^\circ$ of the quarter-wave plate. If light is already linearly polarized the quarter-wave plate will be left in a 0° position. Passed the quarter-wave plate, the polarizing cube beam splitters will direct the vertically and horizontally polarized fractions of the incoming light to the right (Image 1) or left (Image 2) half of the ICCD sensor area.

The choices of the settings of the various wave plates in both arms of the instrument will thus allow any state of light polarization to be selected for the measurements. Details of wave plates settings can be found elsewhere¹³.

The second setup will be called the Dual-Polarization Non-Imaging Lidar setup. In this setup, for any experiment, only one FOV is available. However, through the use of an appropriately set iris, the extent of the FOV may be varied at will for any series of experiments. In the case of this setup, the integration of the energy within the selected FOV is made at once at the surface of the detector.

Figure 2 is a schematic of the Dual-Polarization Non-Imaging Lidar optical setup.

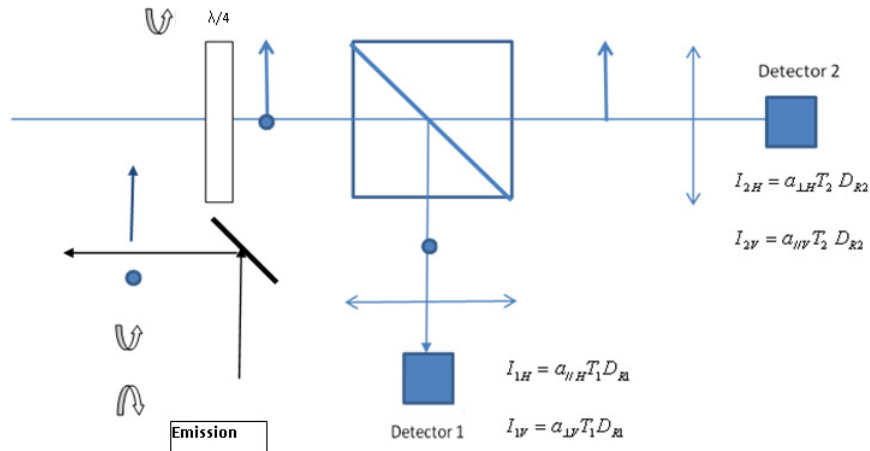


Figure 2: Schematics of the optical layout of the Dual-Polarization Non-Imaging Lidar setup

The emission arm of the instrument is not described in the Figure 2 but it is identical to the one in Figure 1 and will not be discussed here.

The two polarization states are now recorded at two different PMT detectors. The integration of the energy is automatically and instantaneously done at the surface of the detectors themselves. Hence, no calculation needs to be done for retrieving the total energy in each polarization.

The settings of the various wave plates are chosen in the Dual-Polarization Non-Imaging Lidar along the same method as they are done for the MFOV Dual-Polarization Imaging Lidar and will not be discussed again.

The light used in both setups came in four different wavelengths. A first laser source consists of a 100 Hz repetition rate Nd-YAG laser (Solar 629). This laser provides three wavelengths: 355 nm (40 mJ), 532 nm (80mJ) and 1064 nm (200 mJ). The other wavelength of 1570 nm (25 mJ) is obtained from an OPO (Optical Parametric Oscillator) resonator. Beam expanders were used to obtain outgoing laser beams with a 2 cm diameter and a 0.5 mrad divergence (80 % total energy).

In addition to the primary optics, the lidar system is equipped with a 20 cm diameter scanner. This allows to steer the lidar in any direction but it has an effect on the polarization of the light at emission.

The scanner mirrors orientation and its effect on the polarization state of the light emitted by the instrument is illustrated in figure 3.

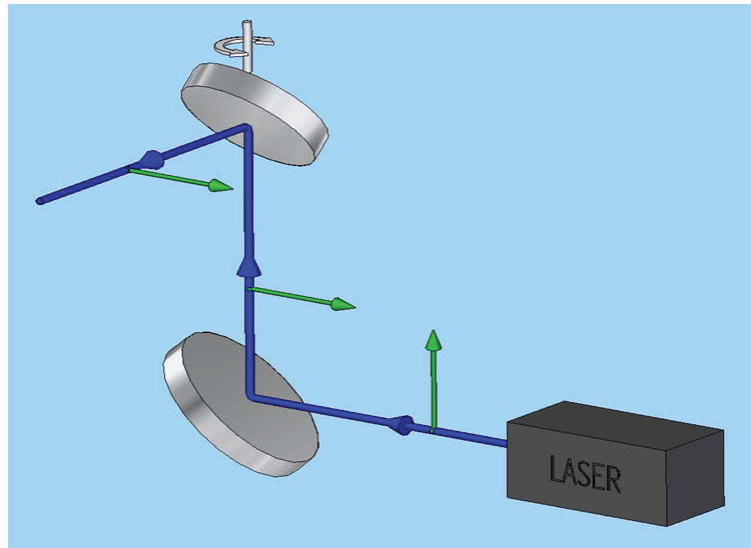


Figure 3: Effect of the scanner mirrors on the polarization state of the light at emission

Mirror reflectivity is not the same for the parallel and perpendicular incident light polarizations. The mirrors are mounted in such a way that the parallel and perpendicular compensate to some extent (parallel incident light is perpendicular on the second mirror and vice versa). Gold coated mirrors have been used for the 1064 and 1570 nm while protected aluminium coating has been used for the 355 and 532 nm. Although it would have been possible to perform measurements at more than one wavelength simultaneously using dichroic optics, single wavelength measurements were performed in order to avoid polarization effects caused by such optics.

It must be noted that, except for the method to be used for integrating the energy over one FOV, all data are processed and treated in the same way whether they originate from the MFOV Dual-Polarization Imaging Lidar or from the Dual-Polarization Non-Imaging Lidar setups.

The data processing is only briefly summarized here as it has been presented at great depth in Cao et al (2010)¹⁴.

The linear depolarization ratio δ_L has been defined as:

$$\delta_L = \frac{P_{\perp}}{P_{\parallel}} \quad (\text{eq. 8})$$

where P_{\perp} is the power received in the detection channel with polarization perpendicular to the polarization state of the light that was emitted and P_{\parallel} is the power received in the detection channel with polarization parallel to the polarization state of the light that was emitted.

The average depolarization ratio can be calculated point by point. However, the synchronization of 2 acquisition channels is not perfect: there is often one digitization bin difference between the two channels. This causes larger variance into the depolarization ratio data. To overcome that problem, it is the ratio of the integrated signal that is calculated.

In the Part II of this paper, relative reflectivity measurements will also be discussed. These data have been acquired with the MFOV Dual-Polarization Imaging Lidar setup with the use of the ICCD camera.

In order to illuminate most of the panel targets, large beam divergence was used. The laser beam could not be considered as being uniformly distributed. To examine the reflectivity of each target, the non-uniformity of the laser beam has to be calibrated. This is called laser beam uniformity calibration.

The laser beam uniformity calibration has been done based on measurement of a homogeneous target which, in the field measurements, was the wooden board supporting the targets. For each polarized (linear horizontal and vertical) light, 5 individual measurements of the homogeneous target were averaged, and the maximum value of the averaged right (image) was used as the reference to calibrate other pixels in this part of the image. The same procedure was applied to the left image. The generated calibration matrix was applied to each target category.

Figure 4 shows comparison of the image intensity of the uniform wooden board target before (4-a) and after (4-b) uniformity calibration. After calibration, the light intensity distribution on the homogeneous target is more uniform than before calibration.

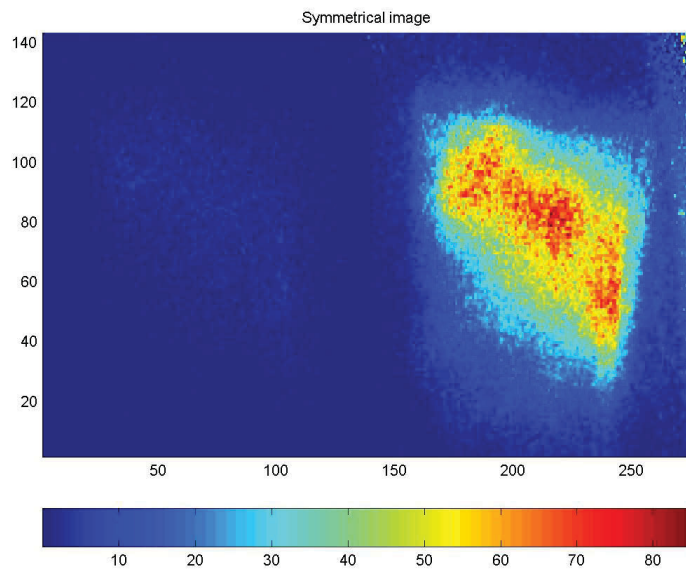


Figure 4-a: Image of the calibration target reflectivity before laser beam uniformity calibration

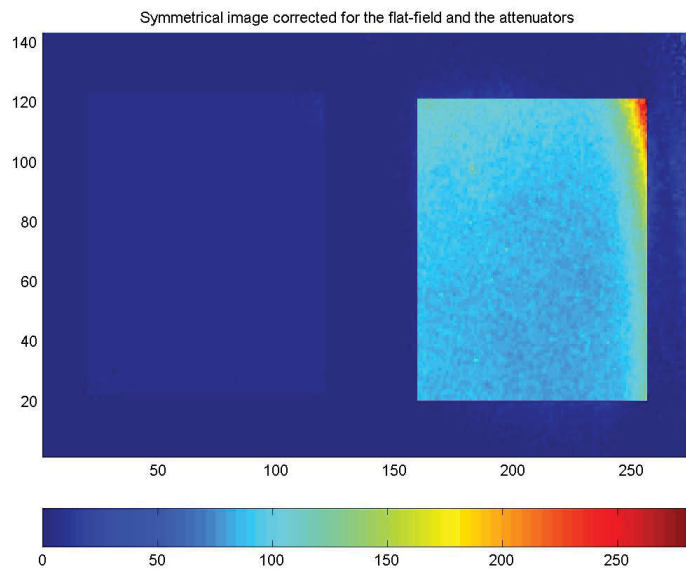


Figure 4-b: Image of the calibration target reflectivity after laser beam uniformity calibration

Relative reflectivity will be used, that is, the ratio of the energy received from some target k to that received from a reference target composed of white Spectralon. Thus, the relative reflectivity is the reflectivity relative to the 99% Spectralon at each incident angle.

$$R_i = \frac{I_i(tot)}{I_r(tot)} = \frac{I_{i\perp}(tot) / n_{i\perp} + I_{i\parallel}(tot) / n_{i\parallel}}{I_{r\perp}(tot) / n_{r\perp} + I_{r\parallel}(tot) / n_{r\parallel}} \quad (\text{eq. 9})$$

where $I_r(tot)$ is the total energy of one pixel of the target received from the reference target r (99% Spectralon), and $I_i(tot)$ is the energy of one pixel received from the subtarget i .

4 SOLID TARGETS FOR LIDAR CALIBRATION

4.1 Background

In this area, the founding paper is the one by Kavaya et al. (1983) [ref. 1]. The work reported in that paper aims at developing a standard sensitivity calibration procedure for lidar equipments to be used for atmospheric aerosol backscatter studies.

Consider some lidar equipment steered at a calibration target located at range R_s and in direction θ . The power collected in backscatter by the lidar detection channel is given by the well-known equation:

$$P_{r,s}(t) = P_t \left(t - \frac{2R_s}{c} \right) \rho^* \frac{A}{R_s^2} \eta O(R_s) e^{-2 \int_0^{R_s} \alpha_s(r) dr} \quad (\text{eq. 10})$$

Where P_t is the time shape and power of the transmitted pulse, A is the area of the collecting aperture, η is the system's optical efficiency, $O(R_s)$ is some range dependent overlap function between the transmission and detection channels and ρ^* is the BRDF of the calibration target.

The above equation can be rewritten in a simplified form as:

$$P_{r,s}(t) = \frac{C}{R_s^2} \rho^* e^{-2 \int_0^{R_s} \alpha_s(r) dr} \quad (\text{eq. 11})$$

in which all the system dependent parameters have been blended into the instrument constant C .

The idea is that, if the atmosphere extinction term $e^{-2 \int_0^{R_s} \alpha_s(r) dr}$ can be estimated (as with the use of a transmissometer for instance) and if the BRDF ρ^* is well known, then the instrument constant C can be measured with great precision. It can be used thereafter to generate the proper aerosol backscatter data inversion.

Kavaya et al. (1983) point at the importance of the selection of the calibration target and of the calibration experimental setup : an ideal target should be easy to fabricate, reproducible, durable and have a well-known BRDF at all wavelengths in the spectral region of interest. [ref. 1, p. 2619]

For most of the solid targets used for this calibration procedure, the assumption is made that the target BRDF is one of a perfect lambertian reflector. The two important features of a true

lambertian reflector are 1) that the reflected radiance is perfectly isotropic and 2) that the light incident at the reflector should be fully depolarized in the reflection process.

In Kavaya et al. (1983), four materials are evaluated with regards to the quality of their lambertian behavior : sublimed flowers of sulfur, flame-sprayed aluminum, 20-grit sandblasted aluminum and 400-grit silicon carbide sandpaper. All four materials are reported as having been used as lidar calibration targets.

The target which best approached the behavior expected from a lambertian reflector was the sublimed flowers of sulfur : the reflectance variation with respect to the angle θ was that of a lambertian to within a worst case error of 10%. Even for this best case, depolarization was never above 30% instead of the expected 100%. The second best depolarizer was the flame-sprayed aluminum at 20%. The other two targets were at 10% at best.

In a paper dated 1987₁₅, Kavaya completely rewrote the calibration procedure in terms of a fully polarimetric pBRDF. It included the Mueller matrix and the Stokes vectors as discussed in section 2. The complete pBRDF approach was to be applied as calibration procedure at the JPL calibration facilities.

In 1989, Haner and Menzies [ref. 2], two of the cowriters of the 1983 paper (Kavaya et al.), applied the JPL full pBRDF calibration method to reevaluate the sublimed flowers of sulfur material used at JPL. Fabrication method had been changed as it seems and depolarization was now nearly complete except in the specular and the backscatter directions, the last of which is of utmost importance in lidar atmospheric studies. They state that the peaks in those two directions could probably never be eliminated, making this best sample still far from a perfect lambertian reflector. With all the other materials they studied, the results were even worst both for the non-isotropy of the reflectance and for depolarization.

They note that the absorption properties at the wavelength of the laser source and the details of the microstructure of the target surface (porosity) determine the details of the depolarization process, which is what the multifacet pBRDF theory is expecting as discussed above.

In the end, their conclusion is that ‘None of the field target materials exhibits good lambertian properties.’

In this part of this paper, depolarization results in the backscatter configuration are given for some materials which are expected to be good diffusing reflectors: Spectralon and some sandpapers.

4.2 RESULTS FOR LIDAR CALIBRATION SOLID TARGETS

The results to be discussed here have been acquired with the Dual-Polarization Non-Imaging Lidar setup used in a backscatter configuration. Here, only the depolarization aspect of the diffusive materials will be discussed.

4.2.1 Spectralon targets

Spectralon® is a pure sintered polytetrafluoroethylene (PTFE) type of material produced and supplied by the company Labsphere. It has been retained as on-board calibration target for the NASA Multi-angle Imaging SpectroRadiometer (MISR). It comes in various grades of reflectivities.

The reflectivities of the materials that have been tested by our team are: 2%, 5%, 10%, 20%, 50%, 75% and 99%. These targets will be referred to as: S02, S05, S10, S20, S50, S75 and S99 respectively. For wavelength dependence of their depolarization quality, all materials have been tested. For the dependence of their depolarization on the incidence angle, only S02, S10 and S99 have been tested.

All the samples had been attached at wooden boards and were located in a chamber located 100 m away from the lidar.

The dependence of the linear depolarization ratio δ_L of the Spectralon targets on the wavelength is shown in figure 5.

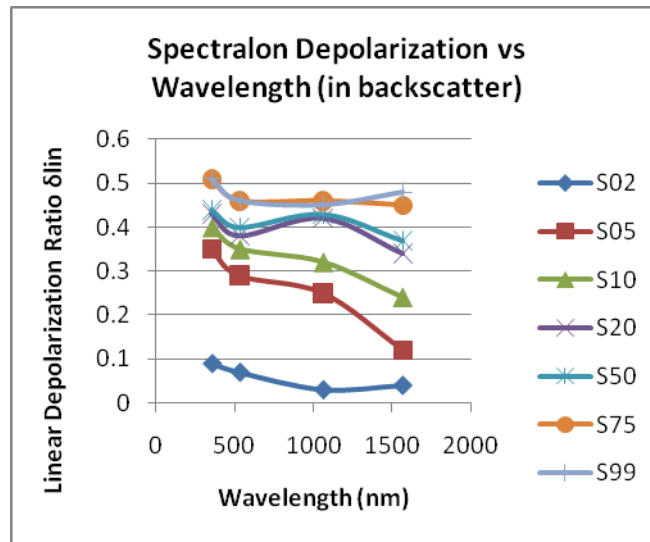


Figure 5: Wavelength dependence of the linear depolarization ratio of various samples of Spectralon materials

With the definition of the depolarization ratio given in equation 8, a full depolarization of light would mean equal intensities collected in Perpendicular as in Parallel polarization channels. As a consequence, the linear depolarization ratio δ_L should be equal to 1.

For the lowest reflectivity Spectralon samples (S02, S10 and S20), the wavelength dependence of the depolarization exhibits the behavior predicted as P1 by the pBRDF theory, that is, δ_L decreases as the wavelength increases. The two highest reflectivity Spectralon samples (S75

and S99) exhibit almost no wavelength dependence, as would be expected from an ideal lambertian depolarizer. The intermediate reflectivity samples exhibit a mixed behavior.

In all cases however, the linear depolarization ratio δ_L is far from the expected value of 1, the closest one being near 0.5 for the S75 and S99 specimen. It is to be reminded here that one major difference between this result and other results acquired elsewhere is that the measurement has been done in a backscatter configuration.

The dependence of the depolarization ratio of some of the Spectralon samples (S02, S10 and S99) on the incidence angle is shown, for each wavelength, in the figures 6-a to 6-d.

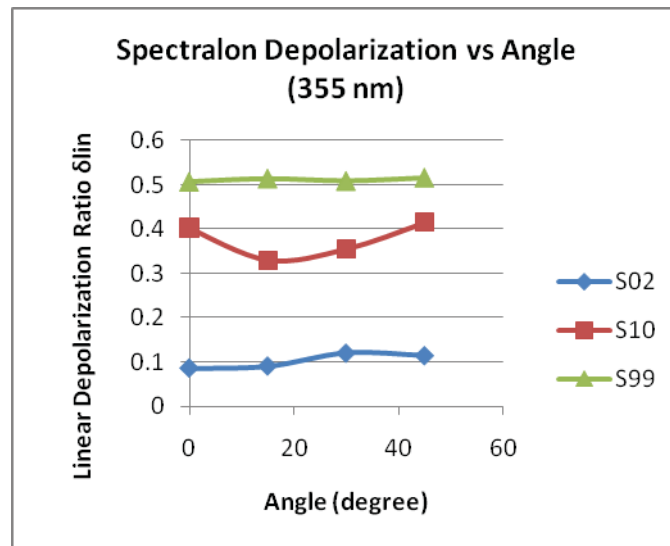


Figure 6-a: Incidence angle dependence of the linear depolarization ratio of various samples of Spectralon materials at wavelength 355 nm

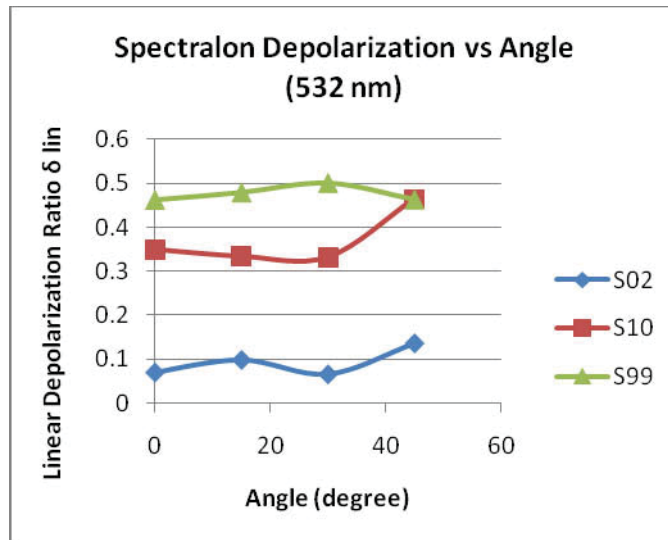


Figure 6-b: Incidence angle dependence of the linear depolarization ratio of various samples of Spectralon materials at wavelength 532 n.

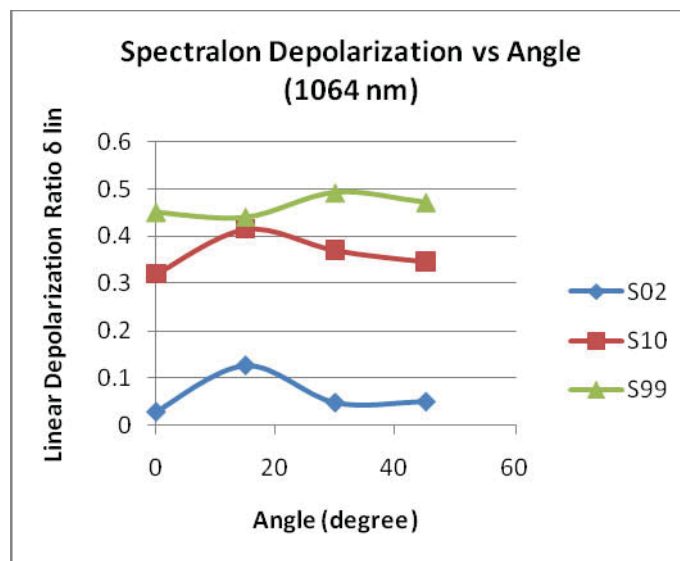


Figure 6-c: Incidence angle dependence of the linear depolarization ratio of various samples of Spectralon materials at wavelength 1064 nm

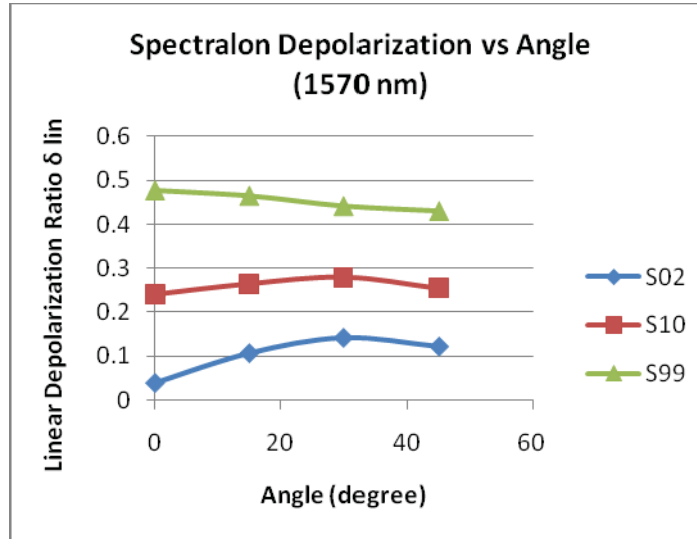


Figure 6-d: Incidence angle dependence of the linear depolarization ratio of various samples of Spectralon materials at wavelength 1570 nm

Here again, only the highest reflectivity specimen (S99) behaves as an ideal lambertian depolarizer and shows almost no angular dependence. The other two specimen show some angular dependence. In all cases where we see a variation of the depolarization ratio with the angle, the variation is consistent with the prediction P4 of the pBRDF theory of an overall increase of the depolarization ratio with increasing angles.

Also, be it for the wavelength dependence or for the angular dependence of the depolarization ratio, the fact that the highest reflectivity sample (S99) comes the closest to being an ideal lambertian depolarizer is also consistent with the prediction P3 of a Umov effect made by the pBRDF theory.

4.2.2 Sandpaper Targets

Various specimen of sandpapers have been measured and analyzed in terms of their eventual use as lambertian diffusers. The specimen selected have grits 50, 100, 220, 400, 600, 1000 and 1500 and will be referred to as SP50, SP100, SP220, SP400, SP600, SP1000 and SP1500 respectively.

The dependence of the linear depolarization ratio δ_L of the sandpaper targets on the wavelength is shown in figure 7.

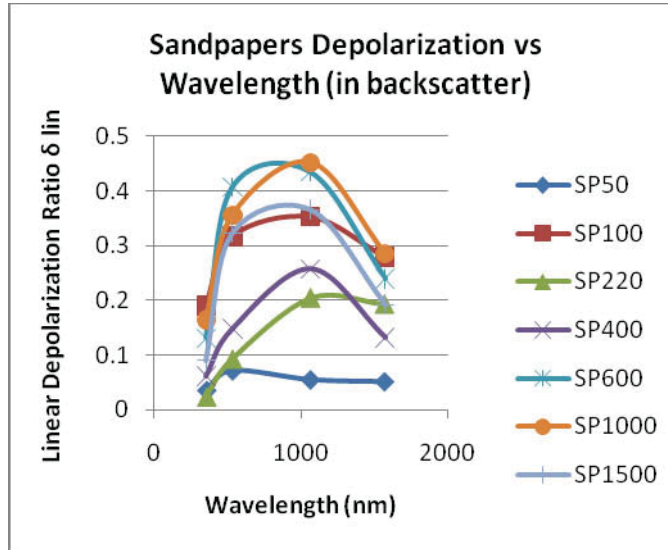


Figure 7: Wavelength dependence of the linear depolarization ratio of various samples of sandpapers.

As can be seen in the graph, the dependence on wavelength does not conform to the prediction P1 of the pBRDF theory. The depolarization ratio starts by increasing from 355 nm up 532 nm and, in some cases, increases again until 1064 nm. It is only after 1064 nm that, for all the specimen, the depolarization ratio decreases. This is in clear contradiction with the pBRDF theory. The specimen that we will study in section 5 of this report will, for most of them, also exhibit the same behavior. In Section 5, after we have shown that this behavior seems to be generalized, we will present a heuristic explanation based on physics principles.

However, for all samples, the prediction P2 is verified as, for every specific wavelength, the depolarization ratio increases as the rms size of the roughness diminishes. It can be seen on the graph that the sandpapers with the highest grit numbers, and thus the smallest surface structure sizes, show the highest depolarization ratios.

The dependence of the depolarization ratio of all of the sandpaper samples on the incidence angle is shown, for each wavelength, in the figures 8-a to 8-d. The prediction P4 is verified: depolarization increases with angle.

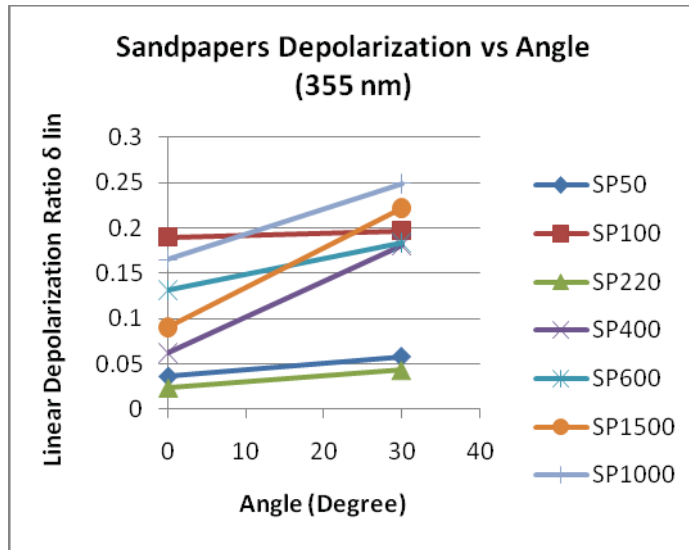


Figure 8-a: Incidence angle dependence of the linear depolarization ratio of various samples of sandpapers at wavelength 355 nm.

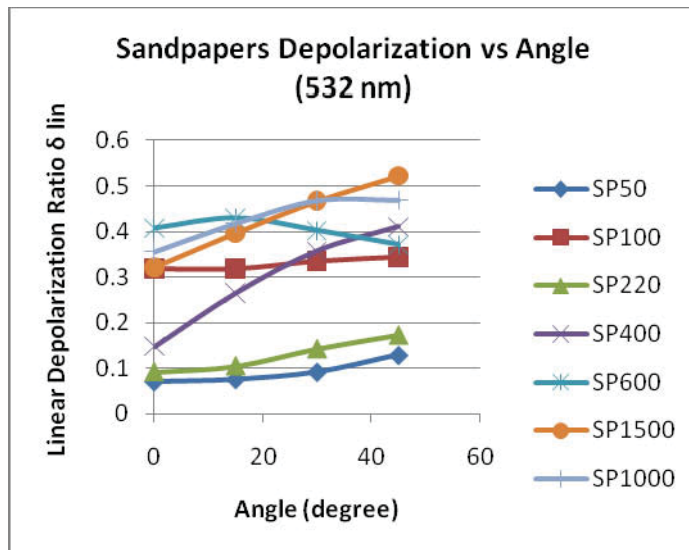


Figure 8-b: Incidence angle dependence of the linear depolarization ratio of various samples of sandpapers at wavelength 532 nm.

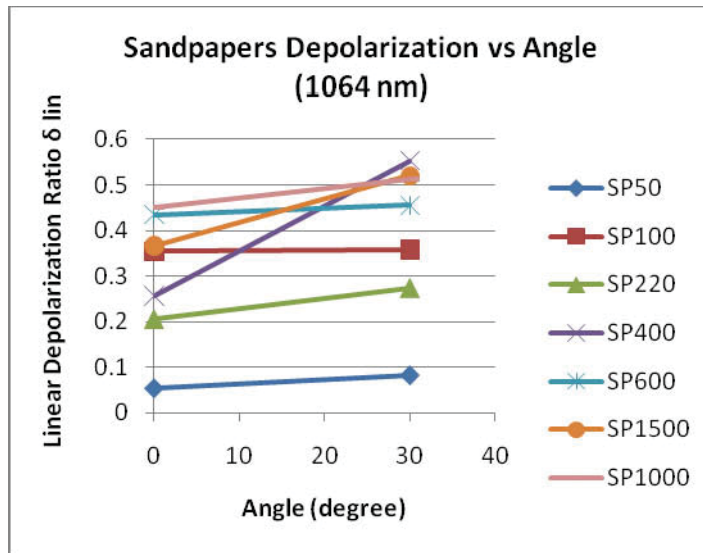


Figure 8-c: Incidence angle dependence of the linear depolarization ratio of various samples of sandpapers at wavelength 1064 nm.

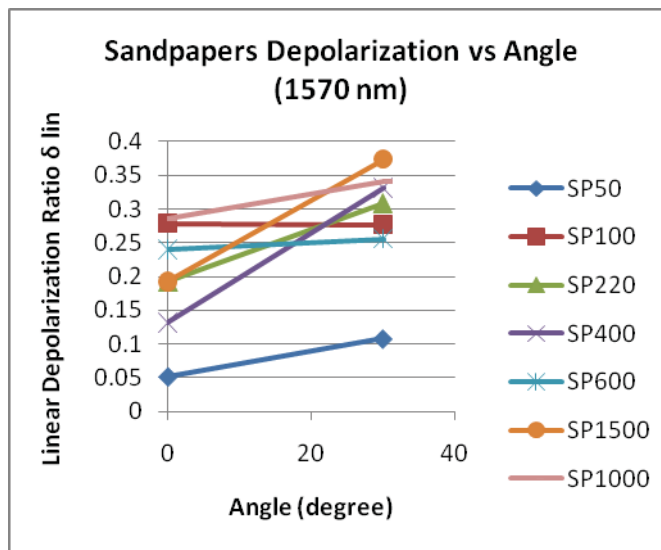


Figure 8-d: Incidence angle dependence of the linear depolarization ratio of various samples of sandpapers at wavelength 1570 nm.

The data collected on these sandpapers with the Dual-Polarization Non-Imaging Lidar setup did not allow us to obtain relative reflectivity data reliable enough to verify whether the sandpaper data obey the prediction P3 of the pBRDF. This prediction is of a Umov effect. However, the very same specimen had been studied at 532 nm with the MFOV Dual-Polarization Imaging

Lidar setup and its ICCD camera which allowed for relative reflectivity measurements. The figure 9 shows the very neat trend of having the depolarization ratio increase with the reflectivity of the specimen. In this figure, some other types of targets than just the sandpapers had also been measured.

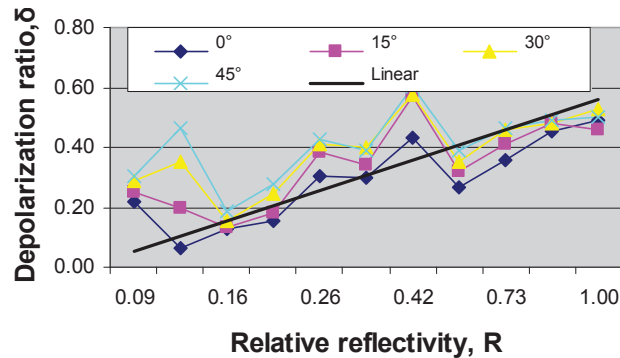


Figure 9: Relationship between depolarization ratio and reflectivity for sandpapers and some other specimen at 532 nm. The figure also shows that the depolarization ratio increases with incidence angle.

4.3 CONCLUSIONS ON HARD TARGETS FOR LIDAR CALIBRATION

The sensitivity of any lidar system to polarization always needs to be quantified. We have shown in an earlier paper¹⁶ that depolarization will be observed even from spherical droplets because of the fact that any lidar has a finite FOV and spherical droplets depolarize at angles close to the backscatter direction. We have also discussed in earlier papers [ref. 13, 14 and 16] the importance of accounting for well-known instrument depolarization effects due to optical components. For these reasons, it is essential that these effects may be precisely quantified and compensated for.

To do this, there is a need for true lambertian reflectors which fully and reliably depolarize light at all wavelengths and all angles.

The results reported here show that no reflector is a true lambertian reflector at least with respect to depolarization. These results further confirm results already reported by other teams.

For atmospheric studies as well as for any other lidar application, it seems essential that facilities like the one at JPL could be used to provide certified and fully characterized reference targets.

5 SOLID TARGETS FOR LIDAR TERRAIN MAPPING AND 3D IMAGERY

5.1 BACKGROUND

Since a ground breaking application demonstration made by Ritchie et al. (1995)¹⁷, the field of laser altimetry and lidar terrain mapping has known important developments. Ritchie et al. had shown that airborne lidar topography could provide important clues for the study of terrain topography and its impact on hydrogeological systems or vegetation patterns.

Kraus and Pfeifer (1998)¹⁸ applied the technology to terrain modeling in wooded areas. They showed that, for that application, the lidar technology was particularly well suited because of its capacity to penetrate the canopy and gather at least some bare earth information, which conventional photogrammetry could hardly succeed at doing.

Since an important review paper by Wehr and Lohr (1999)¹⁹ and another one by Baltsavias (1999)²⁰, the field has known sustained interest. Applications have been multiple since that time: aerial mapping of corridors, roads, railways, coastal areas; glaciers monitoring, measurement of vegetation parameters like canopy height and biomass; urbanistic applications like inventory of buildings in cities.

In a book on Digital Terrain Modeling, El-Sheimy et al.²¹ find many advantages for the lidar technology in that field: because it is an active sensor, it can operate even at night; because of the wavelengths used, it can penetrate the forest canopy; most of all, it will directly provide the 3D elevation information that photogrammetry requires much work to extract from aerial images. The major disadvantage of the lidar technology though is, actually, the fact that it will rapidly provide a huge amount of data whose interpretation is still not yet fully automated.

The lidar cloud of points must first be separated between ground and non-ground points. Most algorithms for doing so are one of three possible types as recently reviewed by Liu (2008)²²: autoregressive type whereby a model of the terrain is first postulated and errors are iteratively diminished; morphological type in which typical image segmentation operations based on geometrical features are applied to the image; and slope-based type in which it is assumed that the gradient of natural terrain slopes is distinctively different than from the slopes of non-terrain objects like trees or buildings. The slope-based methods will work by placing a threshold on slope values so that points sloping under this threshold are deemed to be ground points and others non-ground points. These algorithms may work well on smooth terrains but are reported to behave badly in steep slope areas or, more so, in urban areas. The use of morphological approaches is also reported to present important challenges for building segmentation in urban areas²³. In that last work, the algorithm also starts by using a slope-based method to first classify the points between ground and non-ground.

Related to these difficulties is the practical impossibility at the moment for lidar to extract breaklines from the terrain image on the sole basis of range differences. If breaklines can be identified in an image, thereby segmenting the image between different but connected areas, then an important data reduction may be obtained. At the same time, it can contribute to the solution of the ground vs non-ground classification of the points. Whatever the type of algorithm used, this classification is still far from perfect and still requires manual editing as per Liu's 2008 review of the field.

For that purpose, it has been suggested to add more discrimination features than just the range in the lidar signal. For instance, using a full wave acquisition signal, it has been shown that the temporal width of the returning signal can be used to decrease the errors in the image segmentation and classification of objects²⁴. It has also been demonstrated that keeping and treating the intensity information about the lidar signal does also have the same kind of advantages, still over urban areas²⁵.

In this part of the paper, it is intended to argue that the polarization signature of natural or man-made objects could also be used as an additional discrimination feature in these most demanding classification operations. The presentation will proceed in two steps. First, in the section 5.2, we will investigate the depolarization behavior of multiple materials and attempt to validate the idea that sound physical principles lie at the base of the materials polarization signature and that the user may therefore build some confidence in the information it extracts from it. This will be done by scrutinizing the experimental data and see whether the four predictions made by the pBRDF theory are obeyed. Second, in the section 5.3, we will obtain the polarization signature of many materials and verify whether these are sufficient to discriminate between the various objects.

5.2 RESULTS ON THE pBRDF OF SOME SOLID TARGETS

In this section, we will study the reflectivity behavior of various materials. The aim is to verify that the phenomenology of their reflectivity is consistent with the sound physical principles that are at the base of the microfacet pBRDF theory. First, we discuss the overall methodology. Next, we successively study the dependence of the depolarization on the reflectivity, the incidence angle and then the laser source wavelength.

5.2.1 Methodology

Many tens of different materials samples have been attached to wooden black panels. The panels were mounted one after the other in a chamber located 100 m away from the lidar. The figure 10 gives the example of the panel receiving the insulation materials plus some other specimen.



Figure 10: Wooden black panel with diverse specimen of insulation materials.

In the study of the dependence of the depolarization on the reflectivity, the MFOV Dual-Polarization Imaging Lidar setup was used. On each panel mounted for that part of the study, three locations were left for materials whose reflectivity was used as a reference: one location was empty so we could see the black wooden panel itself, which had been used for laser beam uniformity calibration; the other two locations were left for a 99% Spectralon (S99) and a 2% Spectralon (S02) samples. That study has been made at the 532 nm wavelength only.

In the study of the dependence of the depolarization on the incidence angle and the wavelength, the Dual-Polarization Non-Imaging Lidar setup was used. The four wavelengths (355, 532, 1064 and 1570 nm) were successively used. The panels were mounted with various specimen but no reference samples. On each sample and at each wavelength, 200 signals were acquired and averaged.

Since the content of the panels varied from one type of experience to the next, the list of the specimen mounted will be given separately in the appropriate section.

The details of the data processing were given in the section 3 above.

5.2.2 Results for the dependence of depolarization on reflectivity

Let us recall here that this part of the study has been made at the wavelength 532 nm only. The results reported are only those at 0 degree of incidence.

Seven different panels were mounted with specimen whose types were similar enough to be grouped under the following class names: #1-insulation, #2-woods, #3-metals, #4-environment, #5-sandpapers, #6-composites, #7-sands and grass. The description of the individual samples, referred to as sub-targets, is given in the Table 1.

Table 1: Lists of Targets for the study of depolarization vs reflectivity

Subtarget #	Panel 1- Insulation	Panel 2- Wood
1	Empty	Empty
2	Spectralon of 99% reflectivity	Spectralon of 99% reflectivity
3	Spectralon of 2% reflectivity	Spectralon of 2% reflectivity
4	Blue extruded polystyrene (Styrofoam™)	Pine
5	Pink extruded polystyrene (Styrofoam™)	Spruce
6	White extruded polystyrene (Styrofoam™)	Cherry birch
7	polyurethane foam insulation	oak
8	White styro foam	Horizontal Plywood
9	black styro foam	Vertical Plywood
10	Reflectik™	Oriented strand board
11	Black light Styrofoam	Rip board
12	Beige Styrofoam	Cedar
13	Transparent mini-bubble	Black paper
14	FireProof wool	Asphalt shingles
15	Horizontal Mineral wool	Empty

Cont- Table 1

Subtarget #	Panel 3- Metal	Panel 4- Environment
1	Empty	Empty
2	Spectralon of 99% reflectivity	Spectralon of 99% reflectivity
3	Spectralon of 2% reflectivity	Spectralon of 2% reflectivity
4	Vertical Stainless Steel	Crushed Soda Can
5	Horizontal Stainless Steel	Soda Can
6	Green forest Steel	Polyester
7	Copper	Jute
8	Galvanized Steel	Cotton
9	Light Green Steel	Chiffon
10	Brass	Transparent Plastic Bottle
11	Aluminum	Crushed Transparent Plastic Bottle
12	Sand-blasted Steel	Coloured Plastic Bottle
13	Natural Steel	Beer bottle brown
14	6-volts Batteries (Duracell™)	Beer bottle clear
15	Steel Wool	Empty

Cont- Table 1

Subtarget #	Panel 5- Sand paper	Panel 6- Composite
1	Empty	Empty
2	Spectralon of 99%	Spectralon of 99% reflectivity
3	Spectralon of 2%	Spectralon of 2% reflectivity
4	Sand paper 50	Black Rubber
5	Sand paper 100	Orange Silicone
6	Sand paper 220	Polytetrafluoroethylene (Teflon™)
7	Sand paper 400	Flame Retardant Sheet (Kydex Acrilic PVC)
8	Sand paper 600	High Density PolyEthylene
9	Sand paper 1000	Nema Phenolic (Glass fiber reinforced)
10	Sand paper 1500	Acetal (Delrin™)
11	Paper bag	Opaque Styrene
12	Carton	Sand-Coloured Vinyl
13	Transparent Plastic bag	Plastic Glass
14	White Plastic bag	Polycarbonate resin thermoplastic (Lexan™)
15	Empty	Tarpaulin

Subtarget #	Sands	Construction and grass
1	99% Spectralon	99% Spectralon
2	Coarse sand (dry)	concrete
3	Fine sand (dry)	Asphalt
4	Coarse sand (wet)	Grass 1
5	Dry sand (wet)	Grass 2

Spectralon of 99% reflectivity was used as a reference to calculate the relative reflectivity of the other specimen. For the graphs which follow though, the Spectralon targets reflectivities do not appear. Only the specific specimen under study are displayed in the graphs.

The figure 11 gives the results for Panel 1 insulation materials. A clear trend whereas depolarization increases with reflectivity can be seen. It is prediction P3 of the pBRDF that such a Umov effect should be seen for materials with rough surfaces.

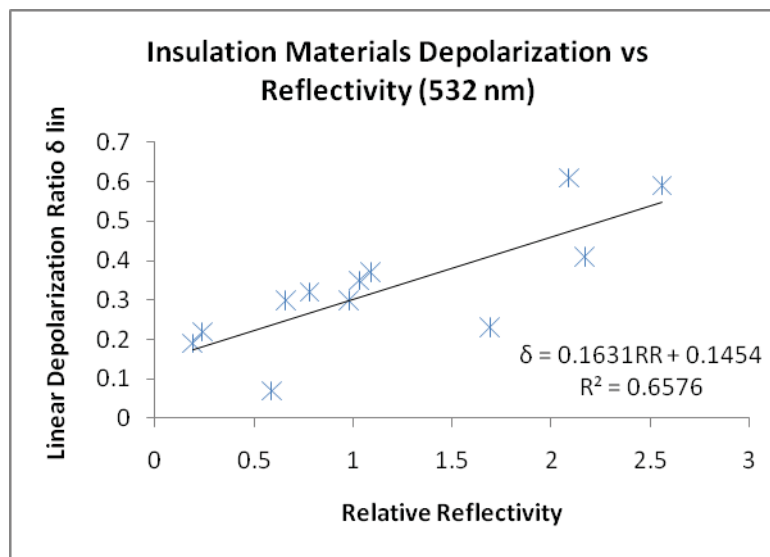


Figure 11: Dependence of the depolarization on the reflectivity of insulation materials at 532 nm.

The figures 12 and 13 give the results for woods and metals specimen respectively. The graphs show no clear trend between depolarization and reflectivity. This is what is expected in the pBRDF for materials where the reflectivity at 0 degree incidence angle is expected to be a first surface reflectivity with thus only a minimum of multiple scattering events.

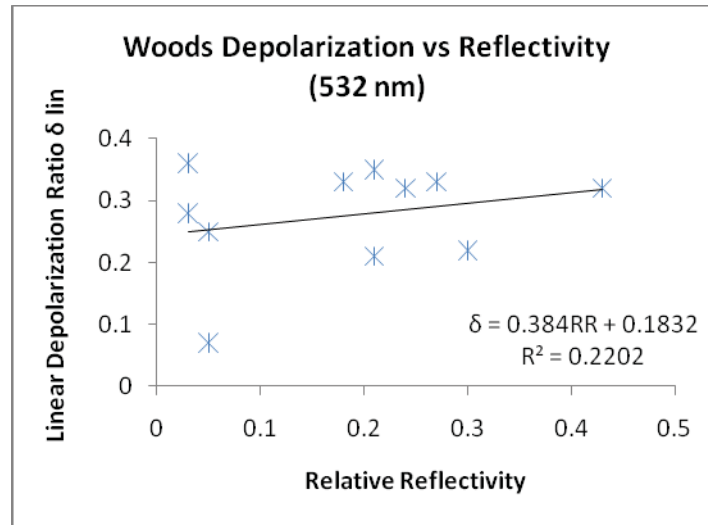


Figure 12: Dependence of the depolarization on the reflectivity of woods at 532 nm.

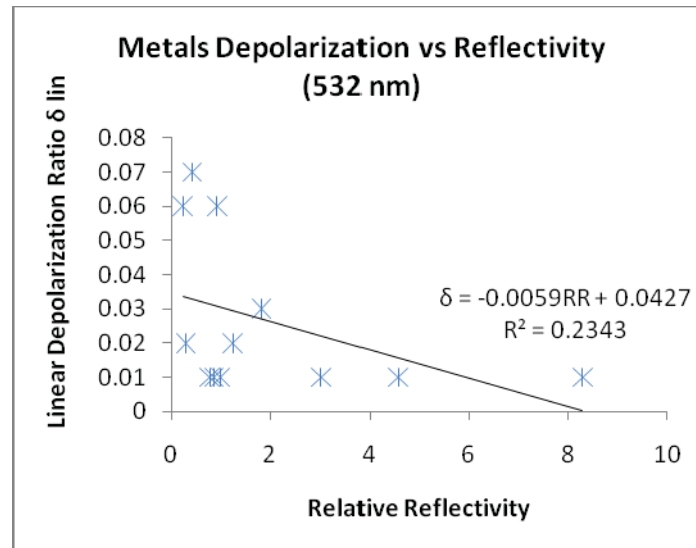


Figure 13: Dependence of the depolarization on the reflectivity of metals at 532 nm.

The figures 14-a and 14-b show the results for the environmental specimen. The figure 14-a, where the graph has been made with all specimen, does not show a clear trend between depolarization and reflectivity. However, if we only remove the sample 5, which actually was a smooth metallic surface soda can, the figure 14-b now shows a very clear trend as predicted by the Umov effect.

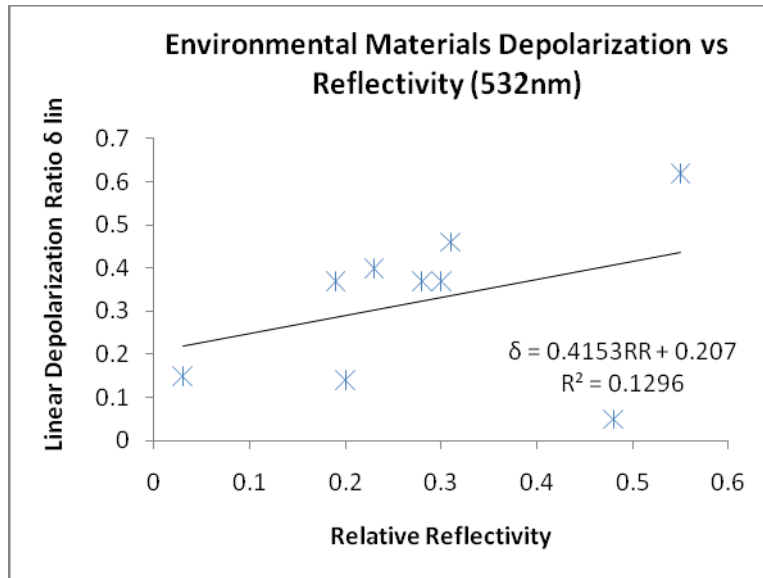


Figure 14-a: Dependence of the depolarization on the reflectivity of environmental materials at 532 nm (all specimen shown).

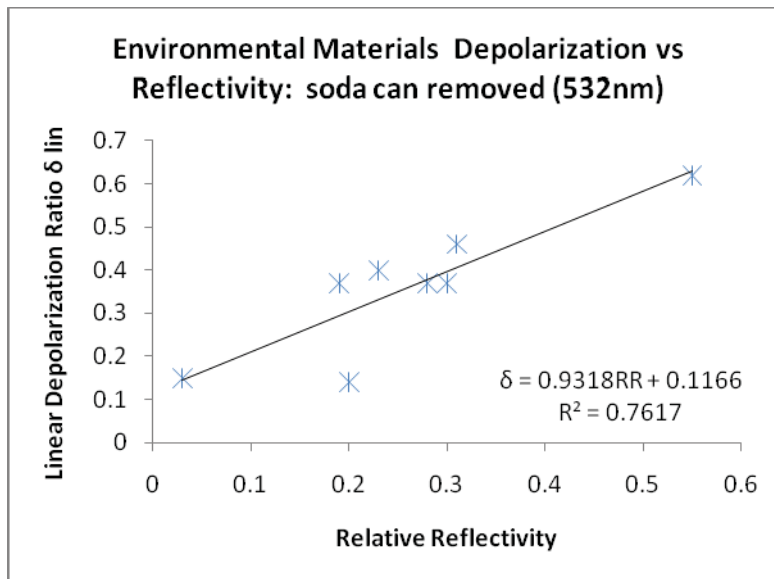


Figure 14-b: Dependence of the depolarization on the reflectivity of environmental materials at 532 nm (smooth metallic soda can, sample 5, removed).

In figure 15, only the specimen 4 to 12 of the Panel 5 named sandpapers are displayed. These are all materials of the same kind : sandpapers, paper and cardboard. The trend is, here again, clear.

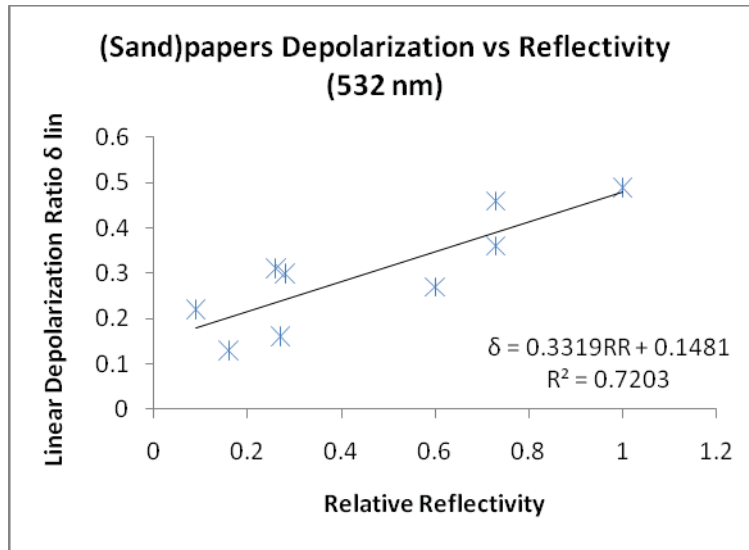


Figure 15: Dependence of the depolarization on the reflectivity of sandpapers, paper and cardboard materials at 532 nm.

The figures 16-a and 16-b give the results for the composites materials. Figure 16-a shows absolutely no trend. Figure 16-b shows the results after having removed the specimen 8 (High density polyethylene) and 9 (Nema phenolic reinforced glass fiber). Even after the removal of these two very dense and smooth surface materials, the trend remains questionable. All those materials are characterized by a rather smooth surface though, which should result in more first surface reflection only.

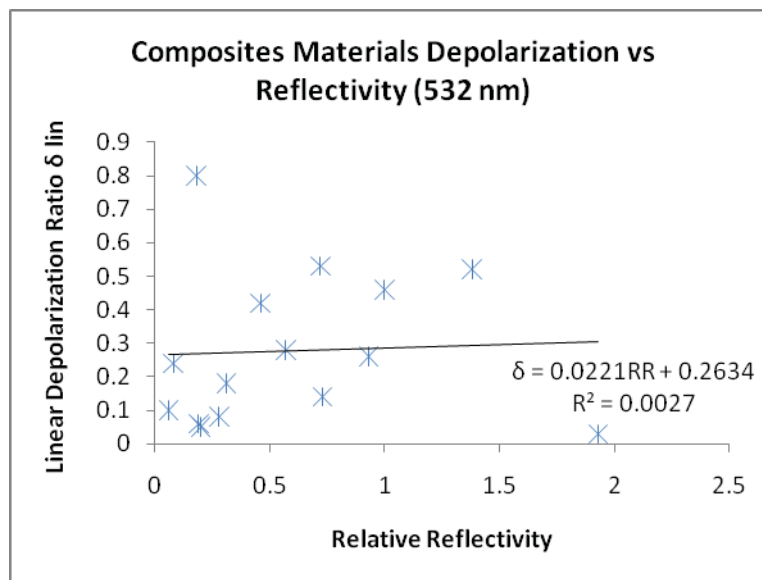


Figure 16-a: Dependence of the depolarization on the reflectivity of composites materials at 532 nm (all specimen shown).

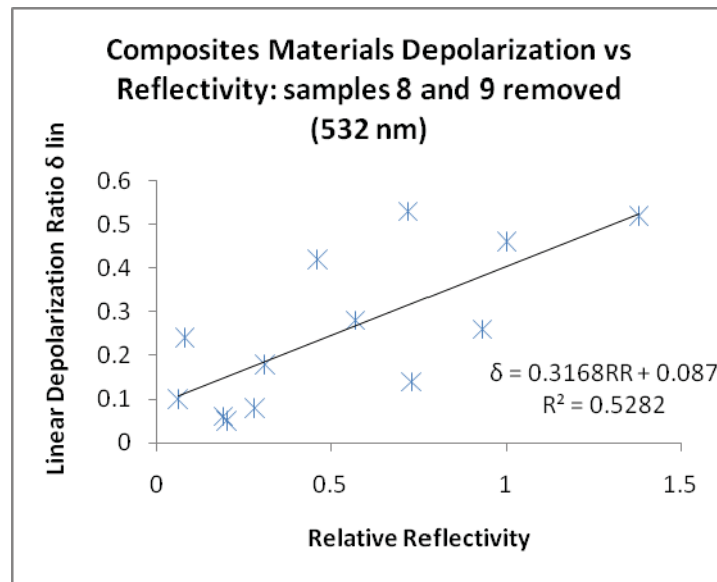


Figure 16-b: Dependence of the depolarization on the reflectivity of composites materials at 532 nm (specimen 8 and 9 removed).

The figure 17 gives the results for some sands and grass specimen. Here again, a trend can be seen between depolarization and reflectivity.

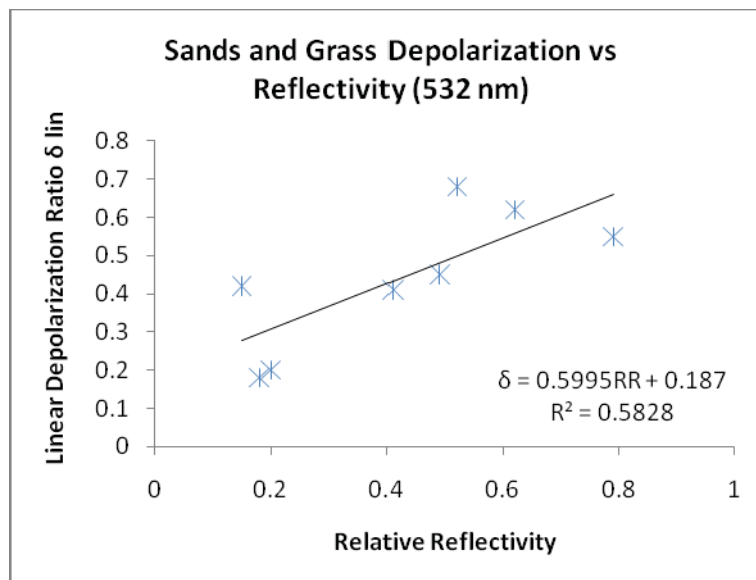


Figure 17: Dependence of the depolarization on the reflectivity of sands and grass at 532 nm.

Overall, the results add up to validate the prediction P3 of the pBRDF theory for 79 out of 82 targets.

5.2.3 Results for the dependence of depolarization on incidence angle

This part of the work, as the following ones, has been made with the Dual-Polarization Non-Imaging Lidar setup at the four wavelengths (355, 532, 1064 and 1570 nm).

Six new panels were mounted : #1-woods, #2-insulation, #3-sandpapers, #4-metals, #5-composites and #6-sands and concrete. The Table 2 gives the description of the specimen for each panel.

Table 2: Lists of Targets for the study of depolarization vs angle and wavelength

Subtarget #	Panel 1- Woods	Panel 2- Insulation
1	Cherry birch	White extruded polystyrene
2	Horizontal Plywood	black styro foam
3	Cedar	Beige Styrofoam
4	Black board	Horizontal Mineral wool
5	Spruce	Pink extruded polystyrene
6	Vertical Plywood	White styro foam
7	Rip board	Black light Styrofoam
8	Asphalt shingles	FireProof wool
9	Pine	Blue extruded polystyrene
A	Cherry birch	Insulation
B	Oriented strand board	Reflectik™
C	Black paper	Transparent mini-bubble

Cont- Table 2

Subtarget #	Panel 3- Sandpapers	Panel 4- Metals
1	Transparent Plastic bag	Green forest Steel
2	Sand paper 1500	Light Green Steel
3	Sand paper 400	Sand-blasted Steel
4	Sand paper 50	Steel Wool
5	White Plastic bag	Horizontal Stainless Steel
6	Paper bag	Galvanized Steel
7	Sand paper 600	6-volts Batteries (Duracell™)
8	Sand paper 100	Aluminum
9	Black board	Vertical Stainless Steel
A	Cardboard	Copper
B	Sand paper 1000	Brass
C	Sand paper 220	Natural Steel

Cont-2

Subtarget #	Panel 5- Composites	Panel 6- Sands and
1	Polytetrafluoroethylene (Teflon™)	Dry dark sand
2	Nema Phenolic (Glass fiber reinforced)	Dry white sand
3	Sand-Coloured Vinyl	Wet dark sand
4	Tarpaulin	Wet white sand
5	Orange Silicone	Concrete
6	High Density PolyEthylene	Asphalt
7	Opaque Styrene	
8	Polycarbonate resin thermoplastic	
9	Black Rubber	
A	Flame Retardant Sheet (Kydex Acrilic	
B	Acetal (Delrin™)	
C	Plastic Glass	

The materials on panels 2 (insulation), 3 (sandpapers) and 6 (sands and concrete) are known to be rough surface materials and good diffusers. For that reason, their depolarization ratio is expected not to show large variation with respect to incidence angle since, even at 0 degree, their reflectance is the result of multiple scattering events. The figures 18, 19 and 20 show the results for all wavelengths.

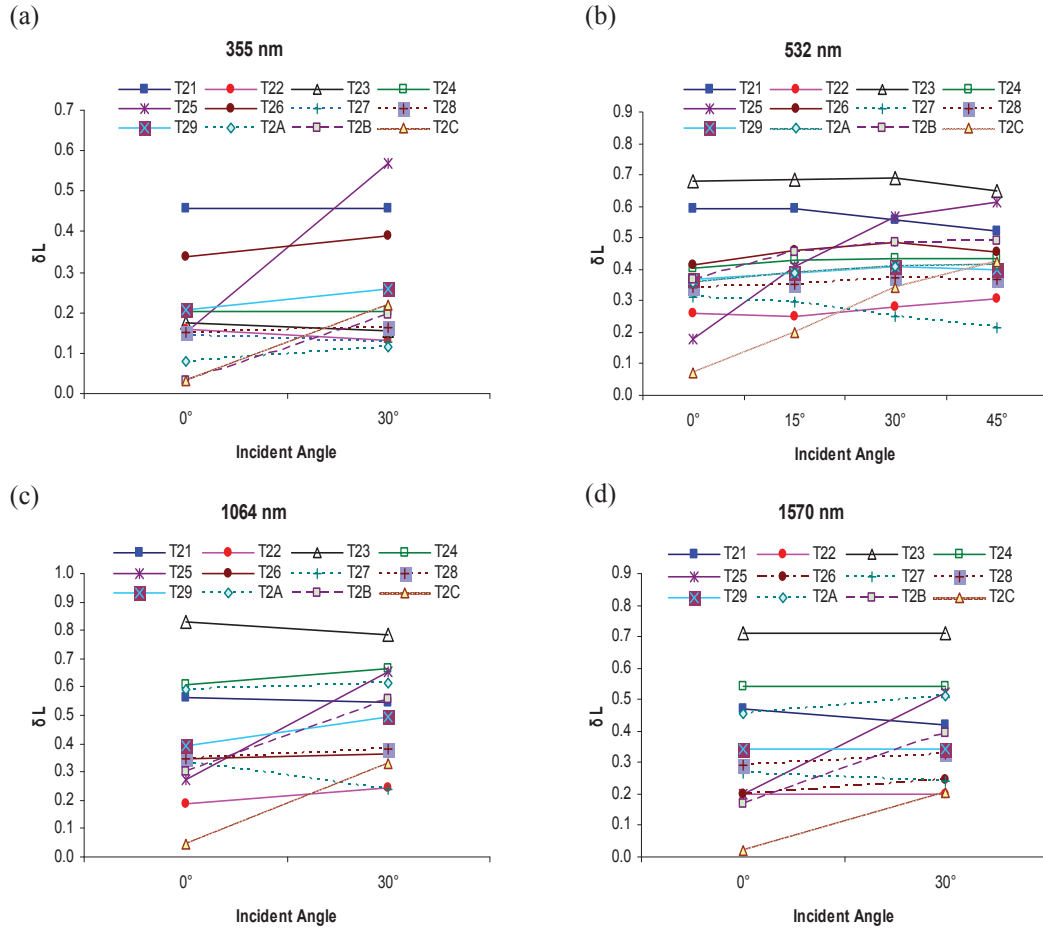


Figure 18: Insulation targets linear depolarization ratio variation with incident angle at each wavelength. (a) 355 nm, (b) 532 nm, (c) 1064 nm and (d) 1570 nm.

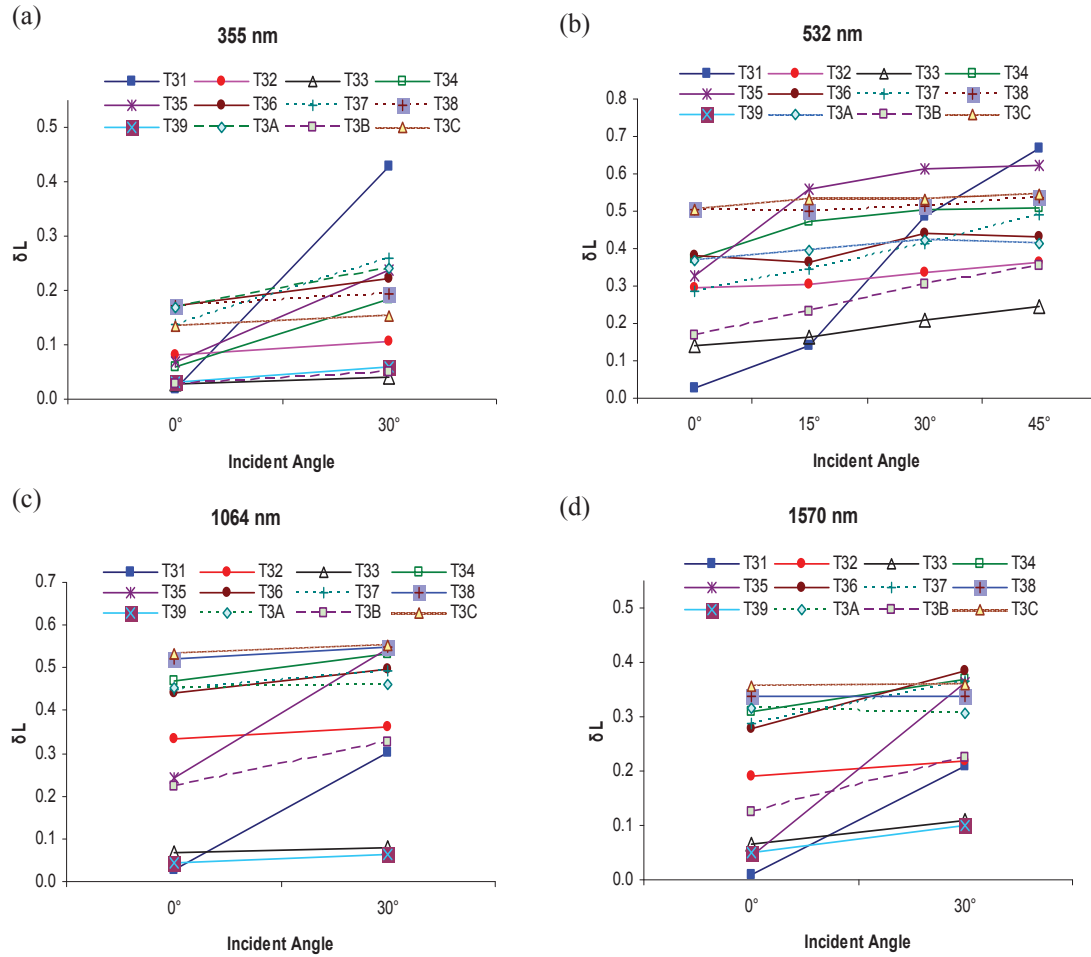


Figure 19: Sandpapers linear depolarization ratio variation with incident angle at each wavelength. (a) 355 nm, (b) 532 nm, (c) 1064 nm and (d) 1570 nm.

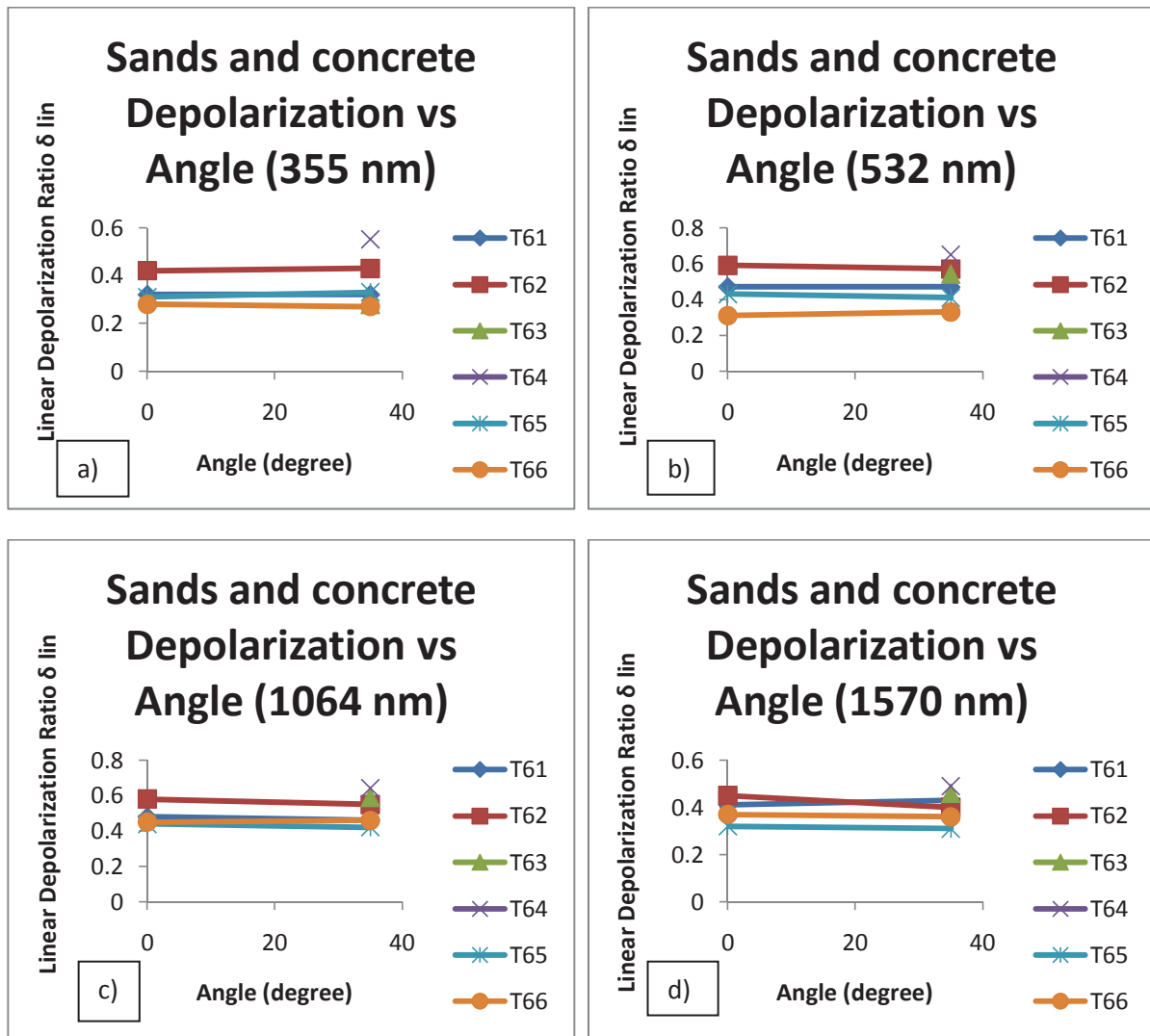


Figure 20: Sands and concrete linear depolarization ratio variation with incident angle at each wavelength. (a) 355 nm, (b) 532 nm, (c) 1064 nm and (d) 1570 nm.

In figure 20, the sands and concrete materials show the expected behavior: no variation. In the figures 18 and 19 though, some specimen show an important variation of their depolarization vs incident angle. These are: specimen T25 (polystyrene), T2B (Reflectik) and T2C (transparent mini-bubbles) from the panel 2 (Insulation); specimen T31 (plastic bag), T34 (sandpaper SP50) and T35 (white plastic bag) from the panel 3 (sandpapers). It must be noted that all of these specimen have smooth shiny surfaces, including the sandpaper SP50 which has the largest surface microstructures among sandpapers. Hence, at angles other than 0 degree, the light returning to the

lidar has to be originating from multiple scattering while, at 0 degree, it must be originating mainly from first surface reflection. This actually is an instantiation of prediction P4.

The materials on panels 1 (woods), 4 (metals) and 5 (composites) are known to have smooth shiny surfaces. For those, we expect large variation of the depolarization with angle for the reason that, at angles other than 0 degree, the light collected at the lidar must have been caused by multiple scattering.

The figures 21, 22 and 23 give the results for the woods, the metals and the composite materials respectively. The prediction P4 is obeyed for most specimen except for some who show almost no variation of the depolarization with angle. These are: T14 (black board), T16 (plywood) and T1C (black paper) from panel 1 (woods); T44 (steel wool) and T4B (Brass) from panel 4 (metals); T52 (reinforced glass fiber) and T58 (thermoplastic) from panel 5 (composites). Among all those 7 specimen which seem not to obey the prediction P4, only the last 3 would require an explanation, the first 4 being truly rough surface materials whose depolarization should not be expected to vary with angle.

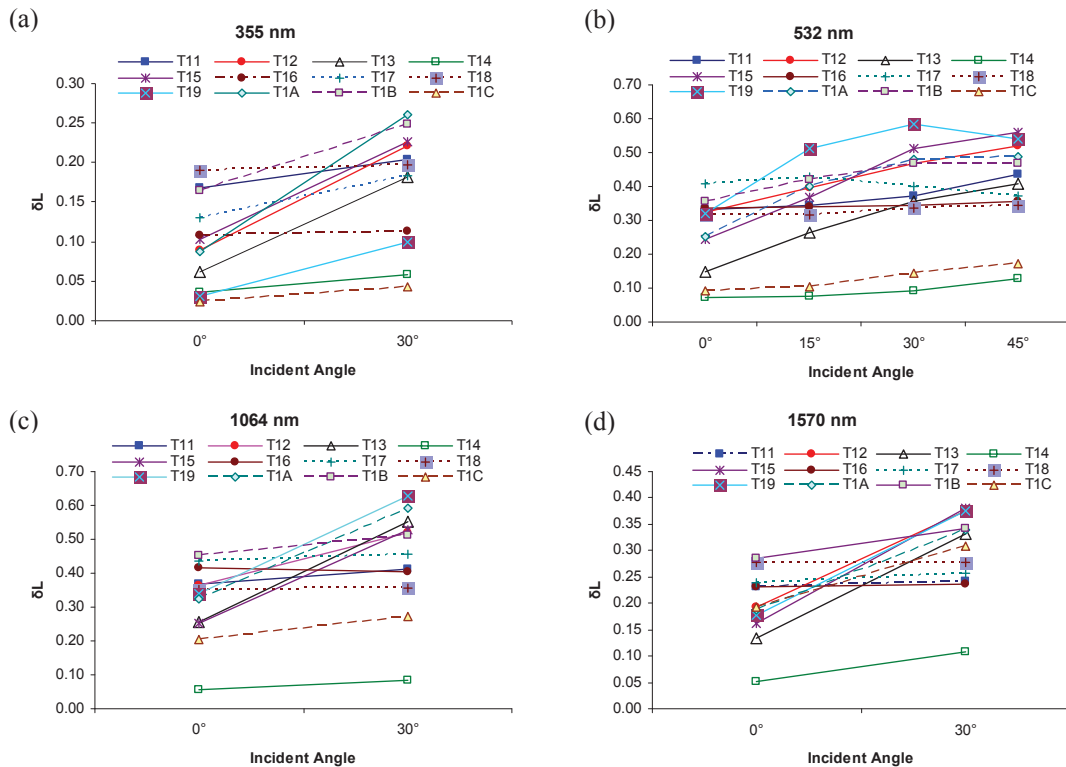


Figure 21: Woods linear depolarization ratio variation with incident angle at each wavelength. (a) 355 nm, (b) 532 nm, (c) 1064 nm and (d) 1570 nm.

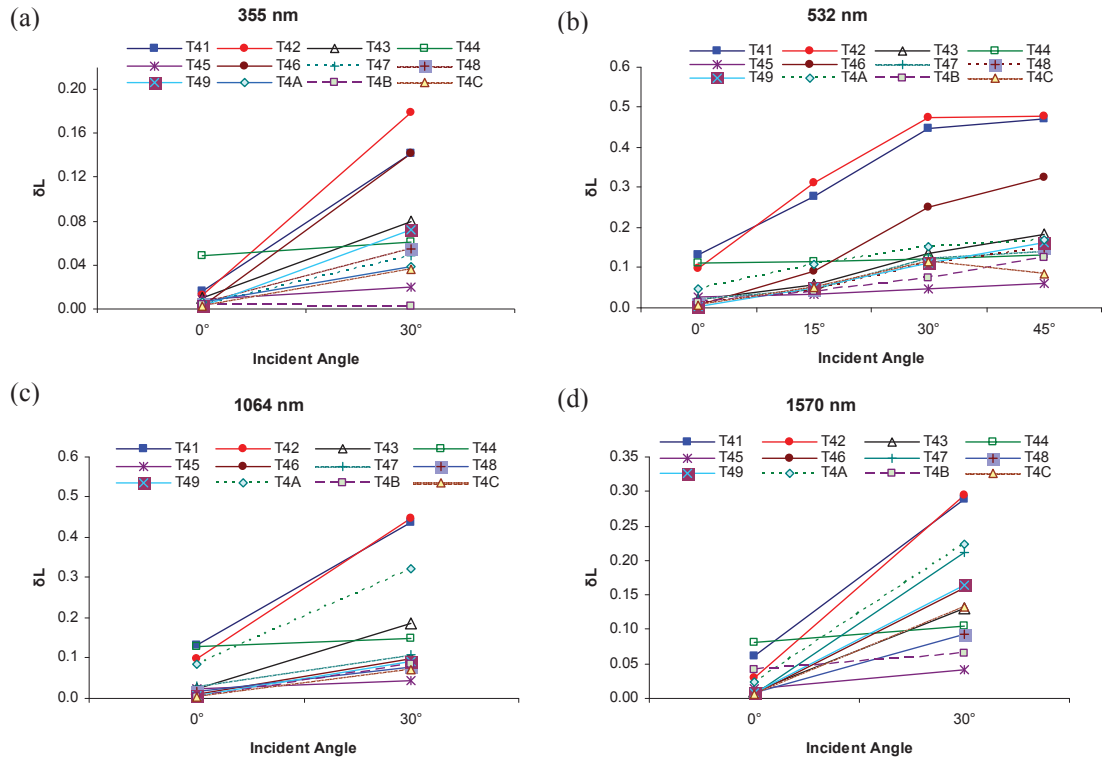


Figure 22: Metals linear depolarization ratio variation with incident angle at each wavelength. (a) 355 nm, (b) 532 nm, (c) 1064 nm and (d) 1570 nm.

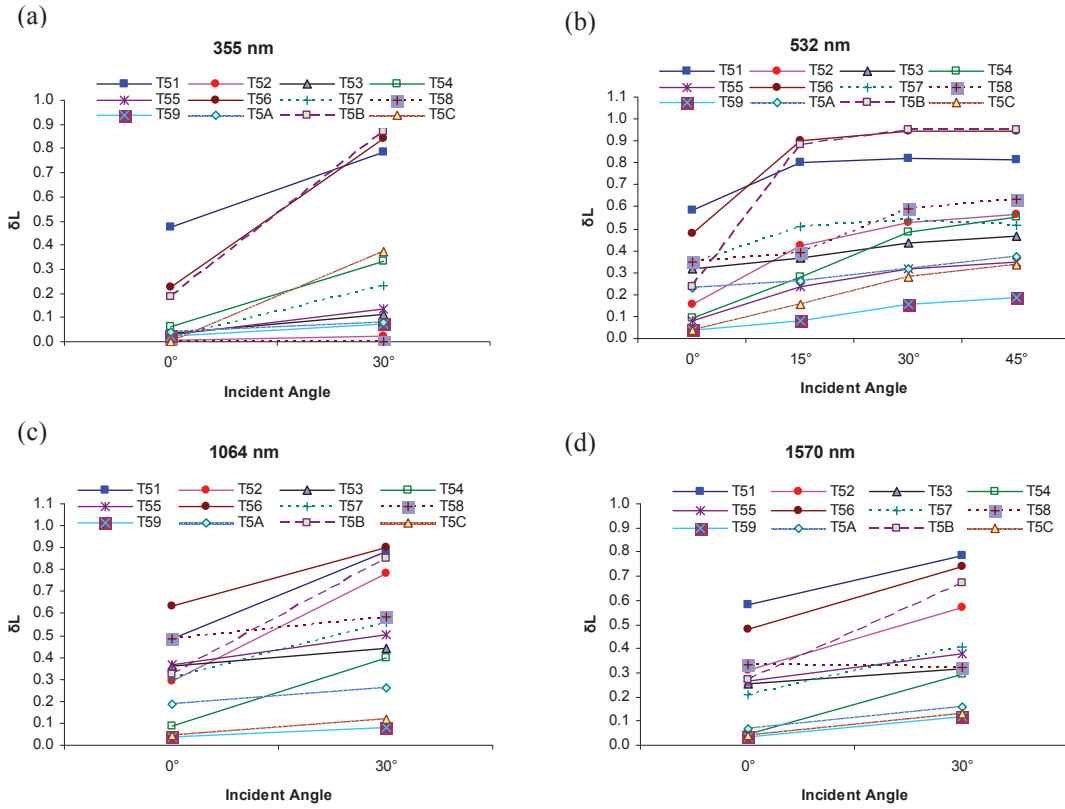


Figure 23: Composites linear depolarization ratio variation with incident angle at each wavelength. (a) 355 nm, (b) 532 nm, (c) 1064 nm and (d) 1570 nm.

Overall, the results add up to validate the prediction P4 of the pBRDF theory for 63 out of 66 targets.

5.2.4 Results for the dependence of depolarization on wavelength

In section 4.2.2, we had reported an important deviation of the behavior of sandpapers with respect to the prediction P1 of pBRDF theory which states that the depolarization should decrease with respect to wavelength. We had observed it instead to increase from 355 to 532 and even to 1064 nm before decreasing to 1570 nm. In almost all the materials that we will consider here, we have observed the very same behavior, and this at the two incidence angles of 0 and 30 or 35

degrees. In what follows, we will first present and briefly comment the results. Then, we will try to explain it from physical principles.

The figures 24 to 29 give the results for Panel 1 (Woods : fig 24), Panel 2 (Insulation : fig 25), Panel 3 (Sandpapers : fig 26), Panel 4 (Metals : fig 27), Panel 5 (Composites : fig 28) and Panel 6 (Sands and concrete : fig 29). Almost all materials strictly obey the prediction P1.

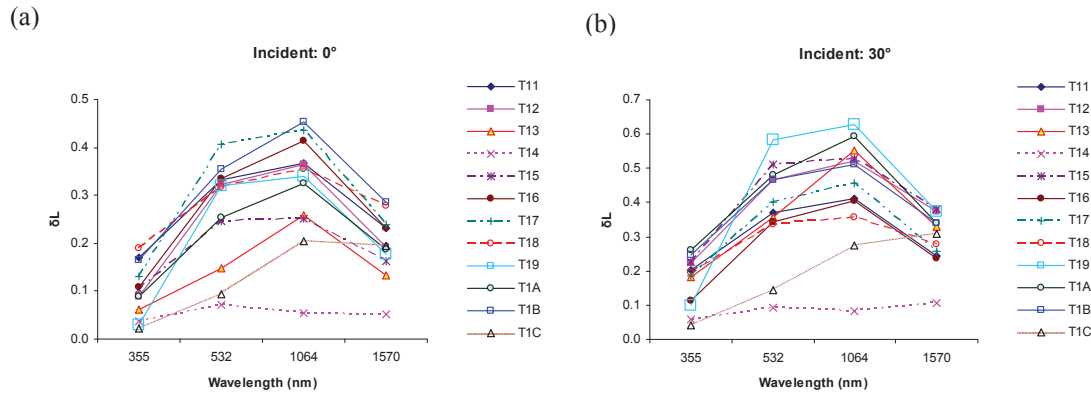


Figure 24: Wood targets linear depolarization ratio variation with wavelength at (a) 0° and (b) 30°

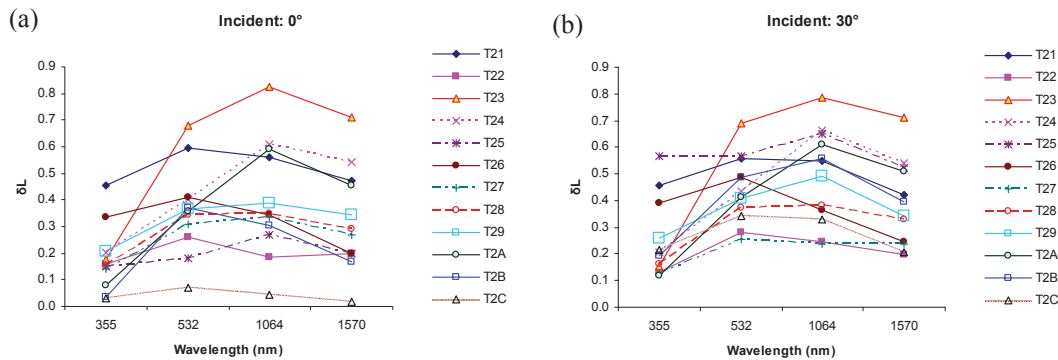


Figure 25: Insulation targets linear depolarization ratio variation with wavelength at (a) 0° and (b) 30°

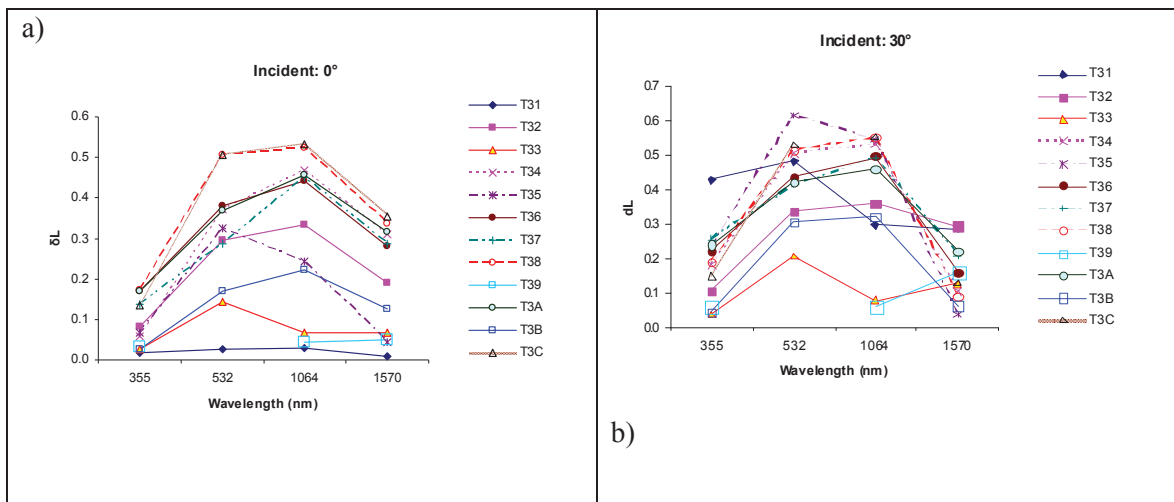


Figure 26: Sandpapers targets linear depolarization ratio variation with wavelength at (a) 0° and (b) 30°

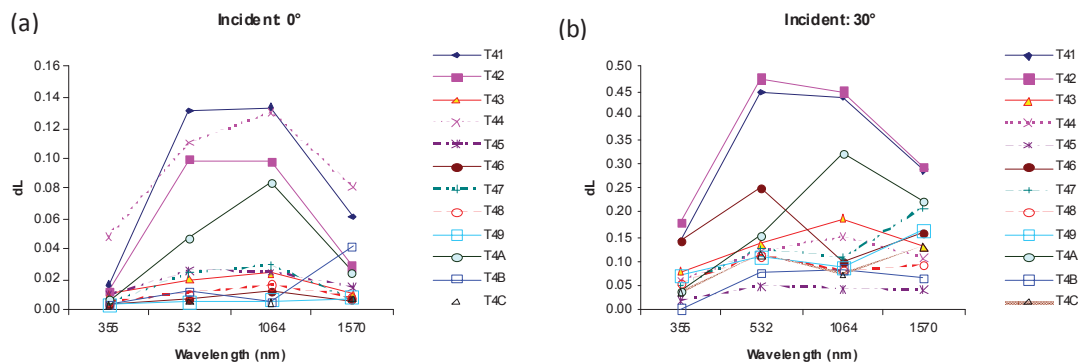


Figure 27: Metallic targets linear depolarization ratio variation with wavelength at (a) 0° and (b) 30°

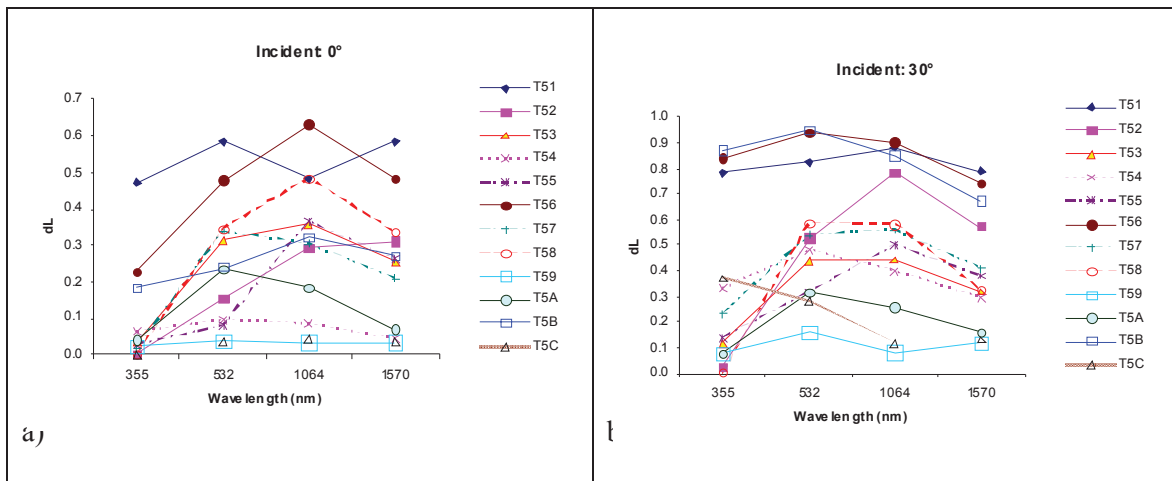


Figure 28: Composite targets linear depolarization ratio variation with wavelength at (a) 0° and (b) 30°

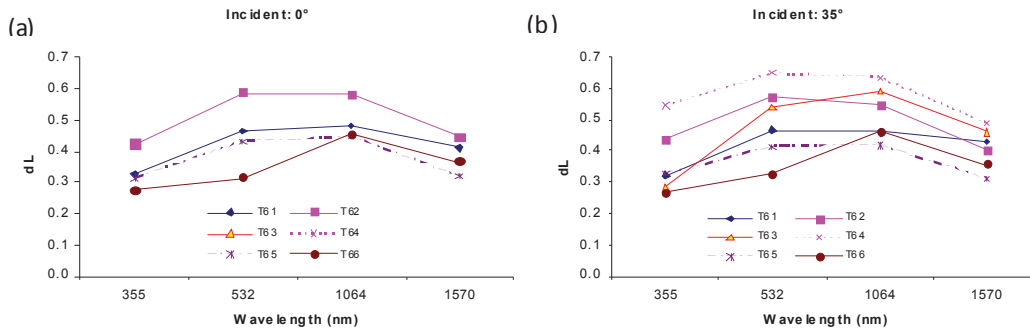


Figure 29: Sands and concrete targets linear depolarization ratio variation with wavelength at (a) 0° and (b) 35°

Some exceptions are: T14 (blackboard), T2C (transparent mini-bubbles), T31 (transparent plastic bag), T59 (black rubber) and T5C (plastic glass). For all of these, we note that the materials are either black and thus highly absorbing at all wavelengths or transparent and thus mainly not interacting with the light.

Some exceptions are: T46 (galvanized steel), T49 (vertical stainless steel) and T4B (brass). For those three specimen, we have found nothing special to explain their unpredicted behavior. But these are 3 specimen out of 66.

We suggest that there may be a physical explanation for this evident contradiction of almost all specimen to the prediction P1 of the pBRDF theory. To explain this widely shared behavior, some other physical principle must be at work at wavelengths smaller than or equal to 1064 nm. What we propose as a heuristic principle is that, at the wavelengths under 1064 nm or 532 nm, higher absorption in the materials would be such as to diminish the occurrence of multiple scattering, thus reducing the depolarization. A Umov effect (prediction P3) would then be counteracting the prediction P1 at smaller wavelengths. This would be consistent with the fact that most solid state materials have wide absorption bands in the UV and Visible parts of the spectrum, due to their atomic electrons.

Overall, the results add up to validate a modified version of the prediction P1 of the pBRDF theory for 63 out of 66 targets.

Actually, what we suggest here as being a modification to the prediction P1 might not even be one. It may already be included in a full implementation of the pBRDF theory. Recall that the equation 7 summarizes the content of the scattering matrix elements as comprising the Fresnel reflectance coefficients among other factors. And the Fresnel reflectance is dependent on the complex index of refraction of the material, which includes the absorption characteristics of the material at each wavelength. A full implementation of the theory, which we have not found trace of in the literature, might well show that the behavior we have experimentally observed is based on a more thorough application of the theory.

5.2.5 Conclusions about the validity of the microfacet pBRDF theory

What the above results suggest is that the predictions that can be made based on the pBRDF theory about the depolarization by solid targets are very generally verified by the experimental data. Depolarization of light by solid targets vary in a predictable way with respect to surface roughness, wavelength, incident angle and reflectivity.

It can be safely thought, then, that depolarization could be used as a discrimination feature in view of recognition and classification of objects in a scene. The next section will address this topic.

5.3 DISCRIMINATION OF SOLID TARGETS BY POLARIZATION

In this part of the report, we aim at answering the question as to whether the depolarization signature of the solid targets can be of use for recognizing the types of objects that are present in a scene in view of their classification and segmentation of the image.

What has been gathered up to now is that the depolarization ratio is sensitive in predicted and reliable ways to surface roughness, wavelength, incident angle and reflectivity. Surface roughness is something the lidar observer cannot control. Hence, we will concentrate on the other parameters.

A statistical analysis tool is required to quantify the difference between each solid target signal. To do so, for a given target 'j', a vector is formed from each of the depolarization ratios obtained at the various wavelengths, incidence angles and/or reflectivities. We are thus building an n dimensional feature space with vectors \vec{p}_j . Depending on how many features are considered, the vectors \vec{p}_j will be of different dimensionality.

The correlation of the different vectors can be calculated as follows: $d_{Euclidean_j,k} = (\vec{p}_j - \vec{p}_k)'(\vec{p}_j - \vec{p}_k)$. However, when doing so, the variance of each measurement is not taken into account, and this could lead to false conclusions regarding whether or not two targets have been discriminated against each other. For example, the distance based on the mean depolarization ratios between two targets could be very large but, if the variance is large also, the two measurements could well be indistinguishable. Also, the distance based on the mean depolarization ratios between two targets could be very small but, if the variance is small enough, the two measurements could well be distinguishable. In calculating the distance between two targets, the variance of the measurements can be taken into account by calculating what is called their Mahalanobis distance.

In the following sections, we will first introduce the basis for the calculations of the Mahalanobis distance. Then, we will present results showing that the various solid targets can be discriminated against each other if the proper feature space is selected.

5.3.1 The Mahalanobis distance

In statistics, the Mahalanobis distance is a distance measure introduced by P. C. Mahalanobis in 1936²⁶. It is based on correlations existing between variables by which different patterns can arise and be analyzed. It differs from the Euclidean distance in that it takes into account the correlations of the data set and is scale-invariant.

Formally, the Mahalanobis distance of a vector $x = (x_1, x_2, \dots, x_N)^T$ from a group of values with mean $\mu = (\mu_1, \mu_2, \dots, \mu_N)^T$ and covariance matrix S is defined as:

$$D_M(x) = \sqrt{(x - \mu)^T S^{-1} (x - \mu)}. \quad (\text{eq. 12})$$

The Mahalanobis distance can also be defined as a distance between two random vectors \vec{x} and \vec{y} of the same distribution with the covariance matrix S :

$$d(\vec{x}, \vec{y}) = \sqrt{(\vec{x} - \vec{y})^T S^{-1} (\vec{x} - \vec{y})}. \quad (\text{eq. 13})$$

In the case at hand here, the vectors \vec{x} and \vec{y} will be any two vectors representing any two different targets.

Assume we have m targets and for each target we have n different measurements. These can be n wavelength measurements, or m_1 wavelengths and $n-m_1$ incident angle measurements or whatever else combination of measurements.

For target i , the multidimensional vector representing the target is :

$$\vec{x}_i = (x_{i1}, x_{i2}, \dots, x_{in})^T, \quad i = 1, 2, \dots, m \quad (\text{eq. 14})$$

If, for instance, 4 wavelengths and only one incident angle measurements are available, then for each target, the total number of possible combinations will be:

$$NN = \binom{4}{1} + \binom{4}{2} + \binom{4}{3} + \binom{4}{4} = 4 + 6 + 4 + 1 = 15. \text{ And the total number of covariance matrix}$$

will be: $m \cdot NN$. For our case, we have 30 solid targets, so the total number of covariance matrices in this case is: $30 \cdot 15 = 450$.

Suppose there are N serial measurements for each target i and the average value of the measurement for target i is \bar{x}_{ij} , $j = 1, 2, \dots, n$. Then the covariance matrix of target i is:

$$S = \begin{bmatrix} \text{Cov}(x_{i1}, x_{i1}) & \text{Cov}(x_{i1}, x_{i2}) & \dots & \text{Cov}(x_{i1}, x_{in}) \\ \text{Cov}(x_{i2}, x_{i1}) & \text{Cov}(x_{i2}, x_{i2}) & \dots & \text{Cov}(x_{i2}, x_{in}) \\ \vdots & \vdots & \ddots & \vdots \\ \text{Cov}(x_{in}, x_{i1}) & \text{Cov}(x_{in}, x_{i2}) & \dots & \text{Cov}(x_{in}, x_{in}) \end{bmatrix}. \quad (\text{eq. 15})$$

Where

$$\text{Cov}(x_{ij}, x_{ik}) = \frac{\sum_{l=1}^N (x_{ijl} - \bar{x}_{ij})(x_{ikl} - \bar{x}_{ik})}{N}. \quad (\text{eq. 16})$$

and

$$\text{Cov}(x_{ij}, x_{ij}) = \sigma_{ij}^2 = \frac{\sum_{l=1}^N (x_{ijl} - \bar{x}_{ij})^2}{N}. \quad (\text{eq. 17})$$

In this work, we have been using a depolarization and/or reflectivity data bank built out of 30 targets at 4 different wavelengths and the covariance matrices of the different wavelength combinations. We have calculated for each target its Mahalanobis distance to all other targets according to equations 13 to 17. And we have identified the unknown target to the data bank target yielding the smallest distance.

The covariance matrices include the effect of the noise in the measurements. As such, they have a direct influence on what the minimal distance between two targets must be if we are to claim that they have been discriminated against. In order to examine the effectiveness of the Mahalanobis distance analysis on target discrimination, measurements with 3 different error sizes were performed: (1) the measurement value is the average value; (2) the measurement value is the average value plus one standard deviation; (3) the measurement value is the average value plus three standard deviations. The measurement with 3 standard deviations represents the possible worst case.

The calculations for a 30 targets data bank lead to a 30×30 Mahalanobis distances matrix wherein the diagonal elements are the distances of each target to itself and in which each row shows the respective distances of the target i to each of the other targets in the data bank. If the diagonal value is the smallest among all those distances, then the target is said to be correctly discriminated from the others. If not, then a discriminating error is produced.

In the next section, we will discuss the results for discrimination between solid targets.

5.3.2 Results for the discrimination between solid targets

The results were acquired with the Dual-Polarization Non-Imaging Lidar setup. The experiment was carried on at the same 4 wavelengths as previously. Some of the targets were moreover looked at from 4 different angles: 0° , 15° , 30° and 45° . For each target, a number of $N=200$ serial measurements were acquired at each wavelength. The average depolarization ratio and the standard deviation, σ , were calculated.

The Table 3 gives the list of the specimen that were used for this experiment. When specimen are named with an H or a V in their name, it is meant that their surface showed polish lines or scratches in either the horizontal or vertical direction.

Table 3: List of Targets for the study of the discrimination possibilities of a polarimetric lidar system

Target #	Material	Material
1	Spectralon 2%	S02
2	Spectralon 5%	S05
3	Spectralon 10%	S10
4	Spectralon 20%	S20
5	Spectralon 50%	S50
6	Spectralon 75%	S75
7	Spectralon 99%	S99
8	Aluminum with horizontal polish scratches	AL1H
9	Aluminum with vertical polish scratches	AL1V
10	Aluminum with horizontal polish scratches	AL2H
11	Aluminum with vertical polish scratches	AL2V
12	Copper with horizontal polish scratches	CU1H
13	Copper with vertical polish scratches	CU1V
14	Copper with horizontal polish scratches	CU2H
15	Copper with vertical polish scratches	CU2V
16	Steel with horizontal polish scratches	ST1H
17	Steel with vertical polish scratches	ST1V
18	Steel with horizontal polish scratches	ST2H
19	Steel with vertical polish scratches	ST2V
20	Blue painted steel	BPST
21	Sandpaper (100 grit)	SP1
22	Sandpaper (100 grit)	SP2
23	Birch wood with horizontal polish scratches	HW1H
24	Birch wood with vertical polish scratches	HW1V
25	Birch wood with horizontal polish scratches	HW2H
26	Birch wood with vertical polish scratches	HW2V
27	Pine wood with horizontal polish scratches	SW1H
28	Pine wood with vertical polish scratches	SW1V
29	Pine wood with horizontal polish scratches	SW2H
30	Pine wood with vertical polish scratches	SW2V

The 30×30 Mahalanobis distances matrices have been calculated using the equations equation 13, and equations 15 to 17, for the following cases: 0 degree incidence angle and only one wavelength (calculated for each wavelength); 0 degree incidence angle and two wavelengths (calculated for all 6 possible combinations of two wavelengths); 0 degree incidence angle and three wavelengths (calculated for all 4 possible combinations of three wavelengths); 0 degree incidence angle and four wavelengths (calculated for the only one possible combination of four wavelengths). Since the measurements had been taken for only a limited number of targets at

angles different than 0 degree, we restricted the calculations to the most demanding case, that is the one where we have the greatest number of targets to discriminate, thus 30 targets at incidence angle of 0°.

The results are reported in the Table 4. In this table, we indicate as wrong discrimination rate, in percent of the total number of different targets, the number of unsuccessful discriminations between any combination of two targets. Note that targets like AL1H and AL2H (or CU1H and CU2H for instance) are treated as being different targets. The values from 1 sigma to 3 sigmas refer to the width of the uncertainty zone surrounding each target. The width of this zone is related to the dispersion between the depolarization values obtained for the target in the $N = 200$ shots that were acquired for it. The smaller the width of that zone, the easier it would appear to discriminate between specimen. And the numbers shown in the Table confirm this intuition.

Table 4: Results of calculations for the discrimination between targets using the Mahalanobis distance

Target discrimination rate		wrong discrimination rate				
wave nb	wavelength	1 σ	1.5 σ	2 σ	3 σ	
1	355 nm	60.00%	76.67%	83.33%	85.00%	
	532 nm	80.00%	86.67%	90.00%	80.00%	
	1064 nm	63.33%	80.00%	80.00%	80.00%	
	1570 nm	80.00%	83.33%	86.67%	78.33%	
2	355+ 532	40.00%	50.00%	63.33%	65.00%	
	355+1064	25.00%	41.67%	51.67%	56.67%	
	355+1570	21.67%	38.33%	55.00%	60.00%	
	532+1064	41.67%	45.00%	51.67%	73.33%	
	532+1570	36.67%	56.67%	66.67%	73.33%	
	1064+1570	33.33%	46.67%	66.67%	56.67%	
3	532+1064+1570	11.67%	61.67%	45.00%	50.00%	
	355+1064+1570	8.33%	55.00%	38.33%	41.67%	
	355+532+1570	13.33%	71.67%	40.00%	60.00%	
4	355+532+1064	18.33%	63.33%	36.67%	51.67%	
	355+532+1064+1570	5.00%	20.00%	31.67%	40.00%	

The wrong discrimination rate remains high until we use the results of at least 3 wavelengths. Then, the best result, at 8.33%, is found for the combination of the wavelengths 335, 1064 and 1570 nm. The 4 wavelengths combination yields only a small improvement at 5%. In both cases, the best result are found when a 1 sigma only uncertainty zone around the target is allowed. This

is not so surprising since many of these targets are very much alike, being all metals in one instance, or all Spectralon materials in another.

This can be visualized in figure 30. In this figure, we have represented the best results obtained in terms of discrimination with only two wavelengths, that is the case of 355 and 1064 nm. We see there that the targets are grouped into types of materials, except for the case of the low reflectivity Spectralon (S02) which seems to be alone of its kind and also for the case of the 100-grit sandpaper SP100, which joins the group of the Pine woods. Within these groups, though, the size of the targets represents their 3 sigma noise. At 3 sigma, many metals are within the uncertainty zone of each other and this is the same for almost all materials.

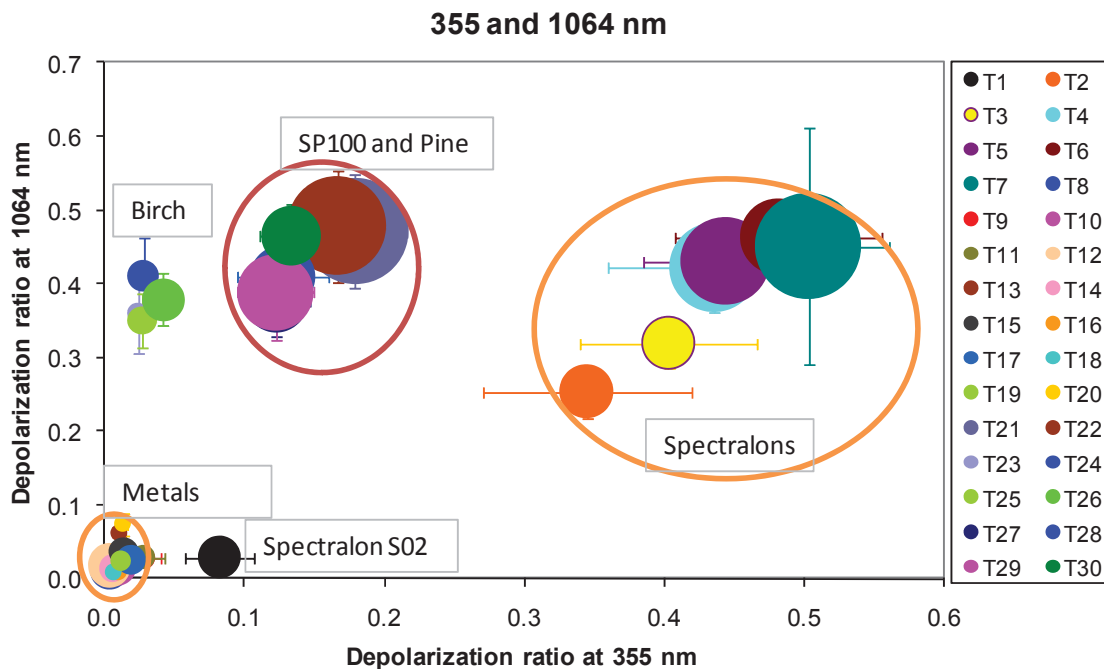


Figure 30: Solid Targets discrimination with two wavelengths

Choosing too large a value for the uncertainty zone thus has the effect of increasing the wrong discrimination rate between targets of the same type.

The Table 5 shows the same data under a different perspective, whereas it is verified rather whether the target has been correctly identified as being part of its own group of material : spectralons with spectralons, metals with metals and so on. There, the best results are obtained at two wavelengths, 355 and 1570 nm where a full discrimination is obtained for 1, 1.5 and 2 sigma noise.

Table 5: Results of calculations for the discrimination between types of materials using the Mahalanobis distance

Material discrimination rate		wrong discrimination rate				
wave nb	wavelength	1 σ	1.5 σ	2 σ	3 σ	
1	355 nm	11.67%	13.33%	21.67%	36.67%	
	532 nm	26.67%	15.00%	23.33%	28.33%	
	1064 nm	25.00%	36.67%	38.33%	46.67%	
	1570 nm	21.67%	26.67%	33.33%	31.67%	
2	355+ 532	0.00%	0.00%	5.00%	10.00%	
	355+1064	0.00%	1.67%	5.00%	11.67%	
	355+1570	0.00%	0.00%	0.00%	5.00%	
	532+1064	8.33%	15.00%	18.33%	25.00%	
	532+1570	11.67%	15.00%	18.33%	20.00%	
	1064+1570	10.00%	21.67%	28.33%	30.00%	
3	532+1064+1570	3.33%	18.33%	18.33%	18.33%	
	355+1064+1570	0.00%	5.00%	1.67%	5.00%	
	355+532+1570	0.00%	6.67%	0.00%	6.67%	
	355+532+1064	0.00%	10.00%	6.67%	10.00%	
4	355+532+1064+1570	0.00%	0.00%	0.00%	6.67%	

It must be noted that, to within some exceptions, the analysis of the Mahalanobis distances matrix shows that the distances are clustered according to groups of materials. For instance, Spectralons have their shortest distances with other Spectralons, metals with other metals and woods with other woods. This is the basis required for the establishment of good classification once a large enough data bank is built. Some exceptions were found though that still require explanation : for instance, the S02 Spectralon was found very close to many woods when only one wavelength was used for the discrimination. This error disappeared when more than one wavelength was used instead. Also, the BPST Blue Painted Steel sample was found to have similarities to some woods in the cases of 2 or 3 wavelengths but not in the other cases of 1 or 4 wavelengths.

From these results, we can argue that the polarimetric lidar could be a valuable tool, adding one more discrimination feature to the lidar signal in view of image segmentation between breaklines and/or classification of the lidar data into ground or non-ground points. The best results are obtained with two and four wavelengths. It must be noted though that the situation might be different with other specimen.

There are good reasons to think that the important point may not be in choosing how many wavelengths anyway but rather in having more than only one feature. We have made our analysis using the depolarization ratio only and have had to look at more than one wavelength to start having better results. But the actual lidar signal already includes at least two other features which

are the range and the intensity. Adding the depolarization ratio as a third one, be it at one wavelength only, could prove of most valuable interest.

6 GENERAL CONCLUSIONS

In this report, we have presented and discussed the results obtained with a polarimetric lidar on solid targets.

In the lidar community, some of those solid targets are seen as potential or actual lidar calibration targets. As such, they are usually assumed to be perfect lambertian diffusers, which include the expectation that they should also be perfect depolarizers. The results presented here, out of many measurements made with at least two different lidar systems, and at multiple wavelengths, show that this expectation is not met.

The other many tens of solid targets specimen observed were only many kinds of materials which could be observed by 3D imagery lidars or by airborne lidars operating as terrain mappers. The aim was to verify whether the polarization signature of solid targets could be added as a discrimination feature for use in the difficult task of automating the processing of the huge amount of data produced by these instruments. It was found that, indeed, polarization would be a specifically material dependent signature and could lead to high discrimination and classification capabilities.

In all, the results have been presented and analyzed under the theoretical umbrella of the pBRDF theory, a short overview of which has been presented also. Our analysis of that theory brought us to outline four predictions that can be made on its basis. These four predictions were challenged by analyzing a great host of experimental data. It was found that they were most generally obeyed. It seems to us that this is a very important result of this report. If the pBRDF theory has been found to be obeyed in a great variety of materials, then we may conclude 1) that the reflectivity and polarization effect of the materials surfaces are predictable and can thus be used as reliable descriptors for most objects and 2) that this theory could be safely and usefully applied for predicting the location and extension of various classes of objects in any feature space that could be built out of it. The existence and definitions of such classes could then be used, in practical applications, to help decide whether one object belongs to one or the other class.

7 References

- [1] Michael J. Kavaya, Robert T. Menzies, David A. Haner, Uri P. Oppenheim and Pierre H. Flamant, , “Target reflectance measurements for calibration of lidar atmospheric studies”, *Appl. Opt.* **22**, 2619-2628 (1983).
- [2] David A. Haner and Robert T. Menzies, “Reflectance characteristics of reference materials used in lidar hard target calibration”, *Appl. Opt.* **28**, 857-864 (1989).
- [3] James R. Shell II and John R. Schott, “Polarimetric Bidirectional Reflectance Distribution Functions (pBRDF)”, chapter 6 in *Fundamentals of polarimetric remote sensing*, SPIE Press, Washington, pp. 63-105 (2009).
- [4] Nonconventional Exploitation Factors (NEF) Modeling, May 2001, ORD 257-96
- [5] K. E. Torrance and E. M. Sparrow, “Theory for Off-Specular Reflection From Roughened Surfaces”, *J. Opt. Soc. Amer.* **57**, 1105-1114 (1967).
- [6] Yinlong Sun, “Statistical ray method for deriving reflection models of rough surfaces”, *J. Opt. Soc. Amer.* **24**, 724-744 (2007).
- [7] D. S. Flynn and C. Alexander, “Polarized surface scattering expressed in terms of a bidirectional reflectance distribution function matrix”, *Opt. Eng.* **34**, 1646-1650 (1995).
- [8] Richard G. Priest and Thosmas A. Germer, “Polarimetric BRDF in the Microfacet Model : Theory and Measurements”, *Proceedings of the 2000 Meeting of the Military Sensing Symposia Specialty Group on Passive Sensors*, **1**, 169-181 (2000).
- [9] John A. Conant and Frank J. Iannarilli Jr., “Development of a combined bidirectional refelctance and directional emittance model for polarization modeling”, *Proceedings of SPIE* **4481**, 206-214 (2002).
- [10] Richard G. Priest and Steven R. Meier, “Polarimetric microfacet scattering theory with applications to absorptive and reflective surfaces”, *Opt. Eng.* **41**, 988-993 (2002).
- [11] B. J. Stagg and T.T. Charalampopoulos, “Surface-roughness effects on the determination of optical properties of materials by the reflection method”, *Appl. Opt.* **30**, 4113-4118 (1991).
- [12] Uri P. Oppenheim and Yoram Feiner, “Polarization of the reflectivity of paints and other rough surfaces in the infrared”, *Appl. Opt.* **34**, 1664-1671 (1995).
- [13] Gilles Roy and Nathalie Roy, “Relation between circular and linear depolarization ratios under multiple scattering conditions”, *Appl. Opt.* **47**, 6563-6579 (2008).
- [14] Xiaoying Cao, Gilles Roy and Robert Bernier, “Lidar polarization discrimination of bioaerosols”, *Opt. Eng.* **49(11)** 116201-1-12 (2010).

- [15] Michael J. Kavaya, "Polarization effects on hard target calibration of lidar systems", *Appl. Opt.* **26**, 796-804 (1987).
- [16] Xiaoying Cao, Gilles Roy and Robert Bernier, "Comparison of the relationships between lidar integrated backscattered light and accumulated depolarization ratios for linear and circular polarization for water droplets, fog-oil and dust", *Appl. Opt.* **48**, 4130-4141 (2009).
- [17] Jerry C. Ritchie, Karen S. Humes and Mark A. Weltz, "Laser altimeter measurements at Walnut Gulch Watershed, Arizona ", *J. Soil and Water Conservation* **50(5)**, 440-442 (1995).
- [18] K. Kraus and N. Pfeifer, "Determination of terrain models in wooded areas with airborne laser scanner data ", *ISPRS Journ. Photogram. Remote Sensing* **53**, 193-203 (1998).
- [19] Aloysius Wehr and Uwe Lohr, "Airborne laser scanning – an introduction and overview", *ISPRS Journ. Photogram. Remote Sensing* **54**, 68-82 (1999)
- [20] Emmanuel P. Baltsavias, "A comparison between photogrammetry and laser scanning", *ISPRS Journ. Photogram. Remote Sensing* **54**, 83-94 (1999)
- [21] Naser El-Sheimy, Caterina Valeo and Ayman Habib, "Digital Terrain Modeling", *Artech House*, Norwood, 2005, p. 50.
- [22] Xiaoye Liu, "Airborne LIDAR for DEM generation : some critical issues", *Progress in Physical Geography* **32(1)**, 31-49 (2008).
- [23] Aparajithan Sampath and Jie Shan, "Building boundary tracing and regularization from airborne lidar point clouds", *Photogrammetric Engineering & Remote Sensing* **73(7)**, 805-812 (2007).
- [24] Gottfried Mandlbürger, Christian Briese and Norbert Pfeifer, "Progress in LIDAR sensor technology – chance and challenge for DTM generation and administration", *Proc. Of the 51st Photogrammetric week*, 159-169 (2007).
- [25] Tuong Thuy Vu, Masashi Matsuoka and Fumio Yamazaki, "Lidar signatures to update japanese building inventory database", *Proc. Of ACRS 2004 Chiangmai Thailand*, 624-629 (2004).
- [26] P. C. Mahalanobis, "On the generalised distance in statistics", *Proceedings of the National Institute of Sciences of India* **2 (1)**, 49–55 (1936).

This page intentionally left blank.

DOCUMENT CONTROL DATA

(Security classification of title, body of abstract and indexing annotation must be entered when the overall document is classified.)

1. ORIGINATOR (Name and address of the organization preparing the document.) Robert Bernier Les instrument optique du St-Laurent 17500 Monté Gascon Mirabel, Québec, J7J 2C5	2. SECURITY CLASSIFICATION (Overall security classification of the document, including special warning terms if applicable.) UNCLASSIFIED (NON-CONTROLLED GOODS) DMC A REVIEW: GCEC JUNE 2010
3. TITLE (The complete document title as indicated on the title page. Its classification should be indicated by the appropriate abbreviation (S, C or U) in parentheses after the title.) <p style="text-align: center;">Lidar Signal Depolarization by Solid Targets and its application to Terrain Mapping and 3D Imagery</p>	
4. AUTHORS (Last name, followed by initials – ranks, titles, etc. not to be used.) Xiaoying Cao and Robert Bernier	
5. DATE OF PUBLICATION (month and year of publication of document.) March2011	6. NO. OF PAGES (Including Annexes, Appendices and DCD sheet.) 74
7. DESCRIPTIVE NOTES (the category of the document, e.g. technical report, technical note or memorandum. If appropriate, enter the type of report, e.g. interim, progress, summary, annual or final. Give the inclusive dates when a specific reporting period is covered.) Contractor Report	
8a. PROJECT OR GRANT NO. (If appropriate, the applicable research and development project or grant number under which the document was written. Please specify whether project or grant)	8b. CONTRACT NO. (If appropriate, the applicable number under which the document was written) W7701-071506
9a. ORIGINATOR'S DOCUMENT NUMBER (Official document number by which the document is identified by the originating activity. Number must be unique to this document.) DRDC Valcartier CR 2011-236	9b. OTHER DOCUMENT NOS. (Any other numbers which may be assigned to this document either by the originator or the sponsor.)
10. DOCUMENT AVAILABILITY (Any limitation on further distribution of the document, other than those imposed by security classification.) <div style="margin-left: 20px;"><input checked="" type="checkbox"/> (x) Unlimited distribution <input type="checkbox"/> () Distribution limited to defence departments <input type="checkbox"/> () Distribution limited to defence contractors <input type="checkbox"/> () Distribution limited to government <input type="checkbox"/> () Distribution limited to Defence R&D Canada <input type="checkbox"/> () Controlled by Source</div>	
11. DOCUMENT ANNOUNCEMENT (Any limitation to the bibliographic announcement of this document. This will normally correspond to the Document Availability (10). However, where further distribution (beyond the audience specified in (10) is possible, a wider announcement audience may be selected.) Unlimited	

12. ABSTRACT (Brief and factual summary of the document. May also appear elsewhere in the body of the document itself. It is highly desirable that the abstract of classified documents be unclassified. Each paragraph of the abstract shall begin with an indication of the security classification of the information in the paragraph (unless the document itself is unclassified) represented as (S), (C), or (U). May be in English only).

Solid targets are used for calibration of lidars for atmospheric studies. Solid targets make up the surface of the Earth and thus they reflect light back to lidars being used for Terrain Mapping. Experience and theory show that if polarization effects are not accounted for in the lidar calibration process, important systematic errors will result. In this report, the experimental study of various solid targets used in lidar calibration shows that none of these truly meets the expectation of being a true lambertian reflector, that is a perfectly isotropically reflector and a totally depolarizing one as well. On another hand, Terrain Mapping, an important lidar application, is still under development. Lidars used in Terrain Mapping yield massive volumes of data. The automatic processing of these data still is an issue and experience shows that adding more features to the lidar signal, over and above the range information, would be a most valuable contribution to automated processing. The work reported in this report is about the use of the polarization signature of solid targets in Terrain Mapping. First, experimental results are compared to the theoretical predictions of the pBRDF theory. The analysis of the results shows that the polarization signature from solid targets may be expected to be a reliable and repeatable feature to add to the data processing. Then, it is shown that discrimination between targets may be obtained by use of their polarization signature. This opens up the way for an improved automation of data processing.

13. KEYWORDS, DESCRIPTORS or IDENTIFIERS (Technically meaningful terms or short phrases characterizing a document and could be helpful in cataloguing it. Should be **Unclassified** text. If not, the classification of each term should be indicated as with the title. Equipment model designation, trade name, military project code name, and geographic location may be included. If possible, should be selected from a published thesaurus. e.g. Thesaurus of Engineering and Scientific Terms (TEST) and that thesaurus-identified.)

Polarimetric lidars, solid targets, calibration, Terrain Mapping, 3D Imagery, polarization signature

Defence R&D Canada

Canada's Leader in Defence
and National Security
Science and Technology

R & D pour la défense Canada

Chef de file au Canada en matière
De science et de technologie pour
la défense et la sécurité nationale



www.drdc-rddc.gc.ca

